Upper Ocean Temperature Variability in the North Atlantic and Southern Oceans: Insights from Adjoint and Forward Modeling

Noah Abner Rosenberg

A dissertation

submitted in partial fulfillment of the

requirements for the degree of

Doctor of Philosophy

University of Washington
2026

Reading Committee:
Daniel Amrhein, Co-Chair
LuAnne Thompson, Co-Chair
Kyle Armour

Program Authorized to Offer Degree:
School of Oceanography

University of Washington

Abstract

Upper Ocean Temperature Variability in the North Atlantic and Southern Oceans: Insights from Adjoint and Forward Modeling

Noah Abner Rosenberg

Co-chairs of the Supervisory Committee:

Affiliate Professor Daniel Amrhein
School of Oceanography

Professor LuAnne Thompson
School of Oceanography

Temperature variability in the upper ocean plays a primary role in global climate, carbon uptake by the ocean, and the general circulation of the ocean, and is therefore a subject of intense study. Changes in the North Atlantic and Southern Oceans are of particular interest due to their importance to global circulation through attempts to understand observed trends and variability over previous decades. In this thesis, we employ and expand a number of methodologies to better understand temperature variability. Chapter 1 focuses on sea surface temperature (SST) variability in the North Atlantic Ocean, where SST proxy records reveal significant heterogeneity in low-frequency variability within the basin. We employ an ensemble of past millennium climate simulations in order to better understand what drives this heterogeneity, finding that some leading dynamical modes can explain part, but not all, of the observed pattern. Chapters 2 and 3 focus on the Southern Ocean and employ an ocean model adjoint to compute optimal atmospheric patterns

that drive variability in the ocean using Dynamics-weighted Principal Component Analysis (DPCA). In Chapter 2, DPCA is used to investigate zonal-mean SST variability, and the results are compared with the role of the Southern Annular Mode, which is the canonical mode of variability in the region. In Chapter 3, we expand the DPCA methodology to account for multiple atmospheric variables, and apply it to understand drivers of zonal asymmetry in the upper 700 meters of the Southern Ocean. Together, these chapters introduce and expand novel methods for better understanding how and why temperature variations arise within the ocean.

Acknowledgements

The work presented here was supported by many individuals and organizations, without whom it would not have been possible. I have immense gratitude toward my advisors, Dan Amrhein and LuAnne Thompson, who provided countless hours of guidance and help over the past six years, from experimental design to writing to navigating the intricacies of academic life. I also thank the members of my committee, Kyle Armour, Evan Solomon, and Cecilia Bitz, for their support in shaping my research and monitoring my progress.

I extend the deepest appreciation for my fiancée, Natasha, for her unwavering support. I would also like to thank my family and friends for truly showing up and having confidence in me in times of stress and uncertainty. Finally, my peers in the School of Oceanography have been an indispensable resource for everything academic and personal, and I would like to acknowledge their contribution to this journey as well.

Contents

Introduction

Upper ocean temperatures play a critical role in climate via air-sea heat exchanges, modulating fluxes of anthropogenic carbon into the ocean, and driving the thermohaline circulation on long timescales (*Gebbie*, 2021). Temperature at a location within the ocean is influenced by several factors: stochastic fluxes from the atmosphere (*Hasselmann*, 1976), advection of temperature anomalies by the ocean circulation, coupled modes of air-sea interaction such as the El Niño-Southern Oscillation (ENSO), and geothermal fluxes. Many studies have attempted to unravel the drivers and signatures of upper ocean temperature variability in an attempt to better constrain past and future changes by using paleoclimate proxy records, theoretical developments, numerical simulations, and direct observations of the ocean.

The chapters of this thesis focus on understanding variability in upper ocean temperatures within the North Atlantic and Southern Oceans using several approaches. In Chapter 1, we investigate power spectra of paleoclimate proxies for Sea Surface Temperature (SST) in the North Atlantic Ocean over the past 1000 years in order to determine time scales of variability at the surface. Finding surprising results from the proxy data, we turn to an ensemble of coupled climate simulations of the same time period in an attempt to understand how the proxies record temperature variance at different spatial points. We employ Low-Frequency Component Analysis (LFCA, *Wills et al.* (2018)) to the ensemble data and adapt it to explore the role of various frequency bands in setting spatial heterogeneity in the power spectra within an ocean basin.

In Chapter 2, we turn our attention to the Southern Ocean, where SST has exhibited surprising temperature variability in the satellite era (1979-present), cooling across several decades while temperatures rose globally. The temperature variability observed over recent has not been replicated across coupled model simulations, leading to a question of what in the atmosphere drives SST that may be missing from models. Previous investigations have explored this question using idealized model simulations (e.g., *Ferreira et al.* (2015)) or analyses of observational data and historical simulations (e.g., *Dong et al.* (2023)). Here, we use Dynamics-Weighted Principal Component Analysis (DPCA, *Amrhein et al.* (2024)) to directly infer drivers of zonal-mean SST in the Southern Ocean using the adjoint to an ocean model, which calculates the derivative of the ocean state with respect to atmospheric fluxes. DPCA reveals that wind stresses over the Pacific play a first-order role in setting the zonal-mean SST.

Chapter 3 expands the DPCA method and explores drivers of zonally asymmetric temperature variability within the upper Southern Ocean, as defined by an index introduced in *Song et al.* (2024). Instead of evaluating atmospheric flux variables (heat flux, wind stress, etc.) individually, we calculate optimal forcing patterns over all atmospheric fluxes simultaneously to capture modes driving the ocean that might exist across co-varying fluxes. We find that two leading modes in the atmosphere control the bulk of asymmetric temperature change. We use perturbation experiments to explore the pathways by which these modes drive changes in the different sectors of the Southern Ocean across seasons. These experiments and analyses reveal that forcing in the Pacific in wintertime, particularly near the Amundsen Sea Low, dominates the signal; however, forcing in the Atlantic-Indian is necessary to account for the full variability.

Chapter 1

Dynamical Drivers of Spectral Heterogeneity and Proxy-Model Disagreement in the North Atlantic Ocean

1.1 Introduction

Estimates of ocean temperature variability at decadal to centennial timescales can provide insight in reconstructing and predicting global and regional climate (*England et al.*, 2014). However, evolution of past temperatures remains poorly constrained by both the observational record and model simulations (*Cheung et al.*, 2017; *Laepple et al.*, 2023; *Laepple and Huybers*, 2014). Because the instrumental record spans only a few realizations of multidecadal variability at best (*Jackson et al.*, 2022), studies of low-frequency variability rely on terrestrial and oceanic temperature proxies. Analyses of sea surface temperature (SST) proxy data from North Atlantic sediment cores suggest that preindustrial SST variability lacks spatial coherence across the basin, a feature attributed to changes in water mass circulation and inhomogeneous patterns of surface variability (*Moffa-Sánchez et al.*, 2019). In addition, covariability between surface properties and circulation metrics such as the Atlantic Meridional Overturning Circulation (AMOC) strength do not always agree between climate models, or between models and proxy reconstructions at these timescales (*Jackson et al.*, 2022).

A useful diagnostic of variability across timescales is the spectral slope β, defined by the power-law relationship for the power spectral density (PSD), PSD $\propto f^{-\beta}$, where f is frequency in years, which summarizes how variance is distributed from high to low frequencies (*Gebbie*, 2021; *Hasselmann*, 1976; *Huybers and Curry*, 2006). Because β compresses the continuum of variability across timescales into a single diagnostic, it provides a powerful tool for constraining estimates of past variability. For instance, a region with anomalously low β has relatively strong high-frequency variance relative to the basin-wide mean, while a high β indicates excess low-frequency variance. *Huybers and Curry* (2006) evaluate β using model, proxy and instrumental data, positing a latitudinal distribution of β whereby the tropical ocean shows values close to 1, whereas the high latitude oceans and land show a value closer to 0. However, there is significant heterogeneity in β in large areas of the midlatitude oceans such as the North Atlantic, as well as uncertainty in β on regional scales (*Gebbie*, 2021). While model and proxy temperature spectra agree well in a globally-averaged sense (*Zhu et al.*, 2019), this agreement breaks down at local and regional scales, where models systematically underestimate multidecadal and longer-period variability when compared to reconstructions from SST proxies and the observational record (*Laepple et al.*, 2023; *Laepple and Huybers*, 2014). A motivating question, therefore, is what physical mechanisms drive variability across timescales, in order to better understand underestimated variance. Furthermore, the agreement on global but not local scales suggests that particular regions may contain underrepresented low-frequency variance, indicating that regional variability is a crucial piece of the mismatch.

We focus on the North Atlantic Ocean, where proxy records with roughly annual resolution are available. These pointwise measurements hold potential insight into regional ocean variability on timescales from years to centuries, but it remains unclear how confidently proxy SST taken at the continental margins (where euch proxies are available) can be extrapolated to the broader basin.

Contributing factors to uncertainty include proxy noise and reconstruction errors (e.g., *Tierney and Tingley*, 2015), as well as uncertainty in the spatial structure of dynamical variability within the region. We first take a set of 15 proxy records of SST with annual-scale time resolution in the past millennium (*Moffa-Sánchez et al.*, 2019) and compute β for each record. We fit β between frequencies of $1/10$ and $1/100$ yr^{-1}, as this band is well resolved by the proxies given 1000 years of annual data. We compare these values to modeled values of β from the Community Systems Earth Model (CESM) Last Millennium Ensemble (LME) (**?**), a 13-member ensemble of historical simulations representing 850–2006 CE. This allows examination of internal variability within the climate system. The ensemble allows us to answer two questions: (a) what role does internal variability, evidenced by the ensemble spread, play in the spatial heterogeneity and uncertainty in β, and (b) do some patterns of SST variability most effectively explain the patterns of β within the area of interest?

We use the LME output to identify dynamical modes of variability from interannual to decadal timescales that most strongly shape the spatial heterogeneity of SST spectral slopes across the basin, under the hypothesis that spatial variations in spectral slope can be ascribed to spatial variations in the imprint of leading modes of SST variability. Modes are identified using both Empirical Orthogonal Function (EOF) analysis (*Lorenz*, 1956) and Low Frequency Component Analysis (LFCA, *Wills et al.*, 2018), which maximizes the contribution of leading modes to variance in a target frequency range. LFCA provides a well-suited tool to study spatial patterns of β, since β is a measure of the ratio of low-frequency to high-frequency variance in a signal, and LFCA identifies modes that dominate the low-frequency variance, which we therefore expect to provide a parsimonious description of the spatial spread in β. We also adapt LFCA to identify modes that prioritize variance in the higher-frequency (0–50 year) band. The log-log scaling of power spectra allows for the possibility that a given amount of variance at high frequency disproportionately steepens or flattens β relative to the same variance at low frequency, but this cannot be determined a priori. By identifying the dynamical drivers of spatial variability in β, we advance interpretations of proxy records, improve model-observation comparisons, and clarify sources of cross-model spread in reconstructed past variability.

1.2 Data and Methods

1.2.1 Proxy Data

We use a set of 15 proxy records for SST in the North Atlantic Ocean, chosen from those discussed in **?**. Proxies are used to reconstruct SST via measuring biomarkers in alkenones (*Sicre et al.*, 2011, 2014), Magnesium/Calcium ratios ((*Moore et al.*, 2017; *Kamenos*, 2010; *Moffa-Sánchez et al.*, 2014)), $\delta^{1}8$O (*Cunningham et al.*; *Sejrup et al.*, 2011), shell growth in bivalves (*Reynolds et al.*, 2013), diatom counts (*Miettinen et al.*, 2012; *Berner et al.*, 2011), and analysis of the composition of plankton assemblages (*Jiang et al.*; *Allan et al.*, 2018). The selected records have at least 50 data points beginning in 1000 CE (Table 1.1), and have mean temporal resolutions ranging from 1 to 12 years. All records are located around continental margins north of 45°N (fig. 1.1a). Different proxies capture SST at different times of the year; however, as this study is concerned with supradecadal variability, we assume they all sufficiently capture the modes of variability on those time scales.

1.2.2 Model Output

Model output is taken from historically-forced coupled runs of the Community Earth Systems Model (CESM) Last Millennium Ensemble (LME), which consists of 13 runs of the CESM 1.1 fully coupled climate model, the ocean component of which is the Parallel Ocean Program (POP) 1-degree model (*Otto-Bliesner et al.*, 2016). A single simulation is run using 1850 CE repeat year conditions and spun up for 650 years, after which 850 CE orbital and greenhouse gas conditions are applied repeatedly and spun up for an additional 1,356 years. After this spinup, differing round-off error perturbations on the order of 10^{-14} °C are applied to the air temperature initial conditions for each of 13 simulations. The same reconstructed aerosol, greenhouse gas, and solar forcings are used for all ensemble members, leaving model spread attributable to internal variability. Averaging across ensemble members yields an estimate of the forced response of climate to radiative forcing. We compute annual average SST from the model output in order to match the highest temporal resolution of sediment records. Additionally, we concatenate the preindustrial (850–1850) portion of the ensemble members to create a 13,000-year record to improve estimates of spectra at centennial timescales. While this creates discontinuities at 1,000-year intervals, this does not meaningfully impact the 10- to 100-year frequency bin of interest.

1.2.3 Orthogonal decompositions

We seek to identify a basis of orthogonal modes that explain spatial variability in the shape of the power spectrum, in order to establish a process-based understanding of spatial variations in β. The procedure to do this is outlined next.

The time series of surface temperature at all points in the basin is represented by a data matrix $\overline{\mathbf{T}}$ with dimensions of space and time. $\overline{\mathbf{T}}$ can be decomposed into a time series of the basin-wide $\mathbf{t}_b$, and a residual $\mathbf{T}$ to give:

$$\overline{\mathbf{T}} = \mathbf{t}_b^T \mathbf{1} + \mathbf{T} \tag{1.1}$$

where $\mathbf{1}$ is a vector of ones spanning the spatial dimension. Notably, as $\mathbf{T}$ can covary with $\mathbf{t_b}$, the spectrum of the lefthand side is not necessarily equal to the sum of spectra on the right. The singular value decomposition (SVD) on $\mathbf{T}$ is given by

$$\mathbf{T} = \mathbf{U}\mathbf{\Lambda}\mathbf{V}^T \tag{1.2}$$

where the rows of $\mathbf{U}$ represent spatial patterns, $\mathbf{\Lambda}$ is a diagonal matrix containing singular values, and the rows of $\mathbf{V}$ contain principal component time series associated with the corresponding spatial patterns. Thus, the SST residual time series at a single point can be described as a sum of spatial weights, eigenvalues, and principal component time series:

$$\mathbf{T}_{i,:} = \sum_j \mathbf{U}_{i,j}\lambda_i[\mathbf{V}_{:,j}]^T \tag{1.3}$$

The Power Spectral Density (PSD) of the time series in eq. 1.3 is evaluated by taking the Fourier transform along the time axis of both sides and squaring its magnitude:

$$\text{PSD} = |\widehat{\mathbf{T}_{i,:}}|^2 = \left|\sum_j \mathbf{U}_{i,j}\widehat{\lambda_i[\mathbf{V}_{:,j}}]^T\right|^2 \tag{1.4}$$

We note that the Fourier transform distributes over addition, and that $\mathbf{U}_{i,j}$ and λ_i are scalars with no time dependence, so equation (1.4) can be written:

$$|\widehat{\mathbf{T}_{i,:}}|^2 = \left|\sum_j \mathbf{U}_{i,j}\lambda_i\widehat{[\mathbf{V}_{:,j}]^T}\right|^2 \tag{1.5}$$

The SVD (eq. 1.2) yields modes that are orthonormal in time, such that $\mathbf{V}^T_{:,j}\mathbf{V}_{:,k} = \delta_{jk}$, and thus by Plancherel's theorem the Fourier transforms of the modes are also orthogonal in frequency space. Therefore, the cross terms in the expansion of equation (1.5) are zero and we can express the spectrum of the full time series as a sum of principal component spectra:

$$|\widehat{\mathbf{T}_{i,:}}|^2 = \sum_j \mathbf{U}^2_{i,j}\lambda_i^2|[\widehat{\mathbf{V}^T_{:,j}}]|^2 \tag{1.6}$$

Equation (1.6) has a useful consequence for the interpretation of spectral slopes in the presence of orthogonal modes of variability: if we regress a mode out of the data matrix $\mathbf{T}$, it removes that mode's variance in every frequency band from the local power spectrum at a point, thereby impacting the local value of spectral slope, with a physical interpretation given by the spatial pattern $\mathbf{U}$, with the caveat that spectral slope is a nonlinear quantity. The most common application of SVD for spatiotemporal data matrices is Empirical Orthogonal Functions (EOFs, *Lorenz*, 1956), which imposes the orthogonality constraint in both time and space dimensions. A modification of this approach is the Low Frequency Component Analysis (LFCA) method (*Wills et al.*, 2018), which maintains orthogonality in time but relaxes the spatial orthogonality constraint. Compared to SVD, the LFCA instead solves for modes that optimize the ratio of variance in a particular frequency band to the total variance of the signal. In other words, we seek orthogonal vectors $\mathbf{U}_i$ that decompose the data matrix such that the following quantity is maximized for leading modes:

$$\frac{(\tilde{\mathbf{T}}\mathbf{U}_i)^T(\tilde{\mathbf{T}}\mathbf{U}_i)}{(\mathbf{T}\mathbf{U}_i)^T(\mathbf{T}\mathbf{U}_i)} \tag{1.7}$$

where $\tilde{T}$ is the SST time series with the desired filter applied, as reconstructed by the leading 30 EOFs, which explain a majority of the SST variance. We refer to $\mathbf{U}_i$ as the ith Low Frequency Component (LFC), and its spatial regression pattern onto the data matrix $\mathbf{T}$ as the associated Low Frequency Pattern (LFP). As we are calculating spectral slope between periods of 10 and 100 years, we investigate the driving modes that influence the various parts of this frequency range, and therefore we use a 50-year, low-pass, fourth-order Butterworth filter to obtain $\tilde{T}$. We also adapt the original LFCA method to derive high frequency components (HFCs) by replacing the low-pass filter with a fourth-order, high-pass Butterworth filter with a critical frequency of $1/50$ yr^{-1}. Similarly, each HFC is associated with a corresponding High Frequency Pattern (HFP) in space.

1.3 Results

1.3.1 Proxy-Model Comparisons

We estimate the power spectral density (PSD) of each proxy using the Thompson Multi-taper Method (*Thomson*, 1982) (Fig. 1.1b) after linearly interpolating between valid data points, and compute β by fitting a line to the PSD in log-log space between frequencies of $1/10$ and $1/100$ yr^{-1} using least squares. Note that as β is a power-law scaling, it is dimensionless. We similarly compute the 10- to 100-year β given by the annual average SST for all ensemble members in the LME in the grid cells closest to the corresponding proxy records (Fig. 1.1c). The proxy-derived β ranges from 0.77 to 3.7, far outside the range of the model ensemble and inconsistent with the established pattern of higher β at lower latitude within the midlatitude to subpolar North Atlantic (e.g., *Huybers and Curry*, 2006). Furthermore, there is significant variability across the proxy records, and only three of the proxy β values are within the model spread for the grid cell at the same location. This introduces two motivating questions: (a) what determines the spatial variations of β within a basin, and (b) what sets the differences in β between ensemble members at the same location within a model? To answer these questions, we focus on LME output as this consists of spatially and temporally complete information.

Table 1.1: List of proxy locations, types, and reconstructed variables with corresponding references.

#	Location (lat, lon)	Archive/Measure	Reconstructed Variable	Reference
1	(47.2, −54.6)	Alkenones	SST	*Sicre et al.* (2014)
2	(55.4, −59.8)	Mg/Ca	SST	*Moore et al.* (2017)
3	(56.0, −5.6)	Mg/Ca	Summer SST	*Kamenos* (2010)
4	(56.0, −5.6)	Mg/Ca	Winter SST	*Kamenos* (2010)
5	(56.6, −6.4)	*G. glycimeris* growth	SST	*Reynolds et al.* (2013)
6	(56.7, −5.9)	Foraminiferal δ^{18}O	SST	*Cunningham et al.*
7	(57.5, −27.9)	Alkenones	SST	*Sicre et al.* (2011)
8	(57.5, −27.9)	Diatom assemblages	August SST	*Miettinen et al.* (2012)
9	(61.5, −19.5)	*G. inflata* Mg/Ca	SST	*Moffa-Sánchez et al.* (2014)
10	(63.8, 5.3)	*N. pachyderma* δ^{18}O	Summer SST	*Sejrup et al.* (2011)
11	(66.6, −17.7)	Alkenones	SST	*Sicre et al.* (2011)
12	(66.6, −17.4)	Diatom assemblages	SST	*Jiang et al.*
13	(67.0, 7.6)	Diatom transfer function	August SST	*Berner et al.* (2011)
14	(68.6, −53.8)	Dinocyst MAT	Summer SST	*Allan et al.* (2018)
15	(68.6, −53.8)	Dinocyst MAT	Summer SST	*Allan et al.* (2018)

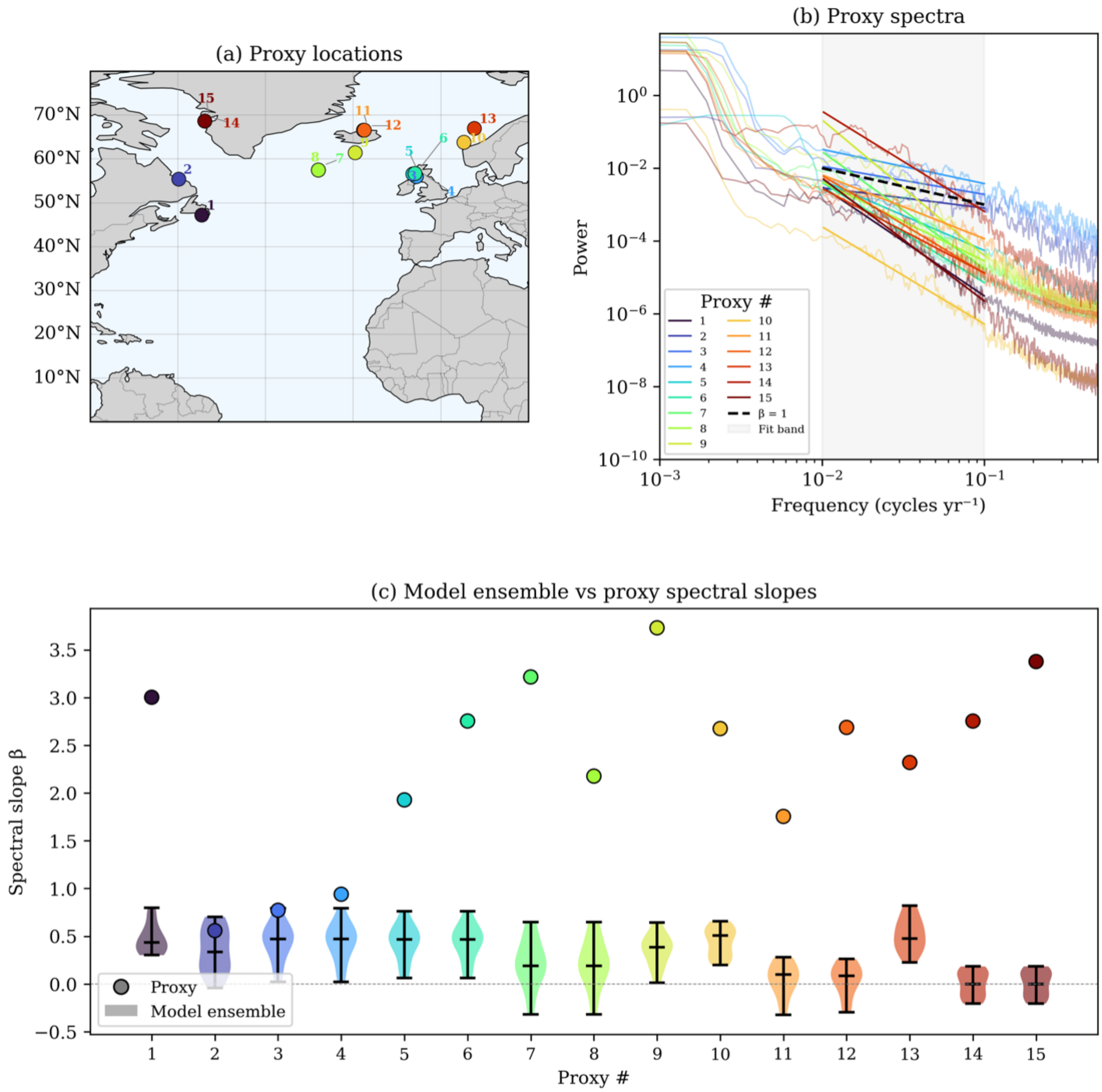

Figure 1.1: (a) Map of proxy locations with labels corresponding to rows in Table 1.1. (b) Power spectra of proxy data with power law fit plotted between 10^{-2} and 10^{-1} cycles/yr (inside gray shading). $\beta = 1$ slope (dashed black line) shown for reference. (c) Ensemble spread of spectral slope at each proxy location from CESM LME (violins) as well as proxy spectral slopes (points). Note that proxies are arranged from lowest to highest latitude.

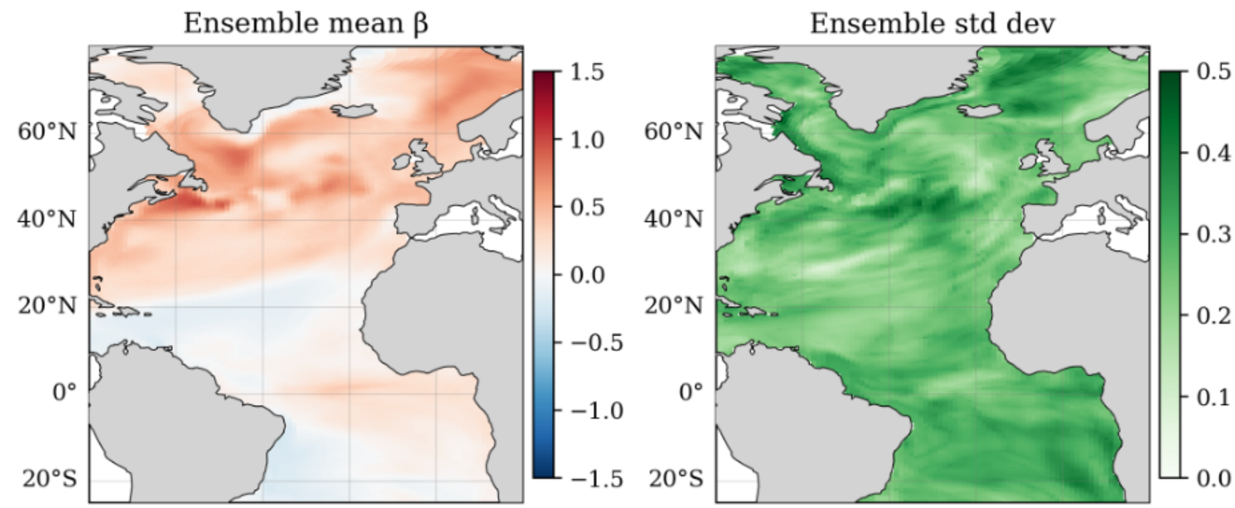

Figure 1.2: Mean (left) and standard deviation (right) across ensemble members of β from sea surface temperature.

1.3.2 Ensemble Statistics

Turning our attention to the model output, we find that the ensemble mean (Fig. 1.2a) shows a sharp contrast between the North Atlantic subpolar gyre (SPG), where β is around 1, and the subtropics where it drops close to zero. Smaller-scale variations are also apparent within the North Atlantic Current (NAC) and SPG regions, where β can vary by as much as 0.5 across distances as small as several hundred kilometers. The ensemble standard deviation (Fig. 1.2b) also displays large variability in β between members of the ensemble within the NAC and SPG regions, reaching 50% or more of the ensemble mean. The large deviations among ensemble members with the same historical forcing and model physics points to internal variability as a strong driver of disagreement in β, potentially leading to disagreement with proxies. As the proxy records contain only a single realization of past climate, in comparison to the model, this is not necessarily unexpected.

1.3.3 EOF and LFC Analysis

Four leading EOF modes (Fig. 1.3a–d) explain a majority of the interannual variability in the North Atlantic SST signal, as calculated from annually averaged SST north of the equator. EOF 1

(Fig. 1.3a) has a horseshoe-like SST pattern in the subtropical and subpolar regions, with positive values in the Greenland-Iceland-Norwegian Seas (GINS) and the Gulf Stream Extension (GSE) region, and negative values elsewhere. The horseshoe SST pattern resembles the canonical SST imprint of the Atlantic Multidecadal Variability (AMV, *Knight et al.*, 2006; *Zhang et al.*, 2019). EOF 2 (Fig. 1.3b) has large magnitudes of SST off the southern and eastern coasts of Greenland as well as to the east of Iceland, while EOFs 3 (Fig. 1.3c) and 4 (Fig. 1.3d) have more complex spatial patterns, with the GINS and GSE regions again showing large magnitudes.

The leading LFPs, which are derived to maximize variance explained at frequencies lower than $1/50$ yr^{-1} relative to total variance, have markedly different patterns than those found in the EOF analysis. LFP 1 (Fig. 1.3e) highlights the North Atlantic Subpolar Gyre (SPG) and GINS, and LFP 2 (Fig. 1.3f) has a more localized pattern off the coasts of Newfoundland, Greenland, and Iceland. LFP 3 (Fig. 1.3g) has large negative values in the GSE region and positive values in the GINS. LFP 4, which explains the most overall variance in SST (29.1%), is mostly localized to the GINS. We note that while the LFPs are ranked in order of their contribution to low-frequency variance, they are not necessarily ordered by contribution to total variance, as can be seen by their total variance contributions in Fig. 1.3.

The HFPs (Fig. 1.3i–l) maximize variance explained at frequencies greater than $1/50$ yr^{-1} relative to total variance. The HFPs show SST magnitude largely confined to the SPG and subtropics, with small amplitude in the GINS, in contrast to the importance of the GINS seen in the other analyses. HFP 1 (Fig. 1.3i) shows an SST imprint in the subpolar gyre. HFP 2 (Fig. 1.3j) somewhat resembles the horseshoe pattern seen in EOF 1, albeit with smaller magnitude in the GINS. HFP 3 (Fig. 1.3k) has positive SST in the southern part of the subtropical gyre and along the GSE, with negative amplitude elsewhere, and HFP 4 (Fig. 1.3l) represents a highly concentrated band of SST variability off the southern tip of Greenland.

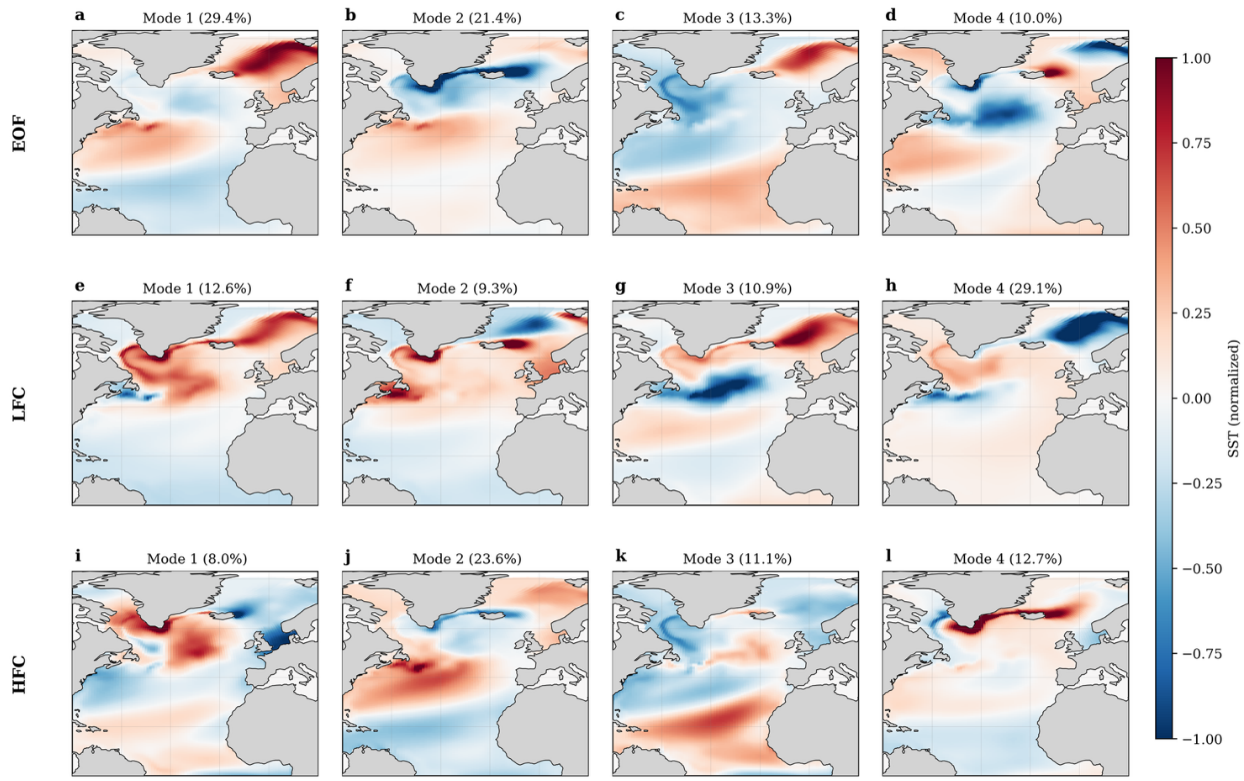

Figure 1.3: Spatial patterns corresponding to leading four modes from EOF (a–d), LFC (e–h), and HFC (i–l) decompositions. Percent of total SST variance explained by the mode is shown in parentheses above each pattern. Note that because LFC (HFC) modes are ranked by percentage of low-frequency (high-frequency) variance explained, they are not generally ranked by percentage of total variance explained.

1.3.4 Contribution of Modes to Spectral Slope Heterogeneity

In order to assess the contributions of leading modes of variability to the spatial heterogeneity of spectral slope β, we iteratively regress out the first N leading modes of each decomposition method (EOFs, LFCs, HFCs) from the stacked SST output with the spatial mean removed ($\mathbf{T}$ matrix from equation 1.1) for $N = \{1, 2, \ldots, 10\}$, and recalculate β pointwise. The resulting maps of β are shown in Fig. 1.4a–l, with the variance in β remaining after each removal plotted in Fig. 1.4m. Removing the first two EOFs reddens the SST (i.e., increases β) in the southern part of the subtropical gyre (Fig. 1.4a,b), lowering the overall spatial variance in β from 0.039 to 0.029, a decrease of 24%. However, subsequent modes removed do not appreciably reduce the spatial variance in β, and removing EOF 3 in fact increases the variance (Fig. 1.4m). Removing the first four LFC modes, in contrast, shows a whitening of SST (lower β) in the subpolar regions (Fig. 1.4e–h), as is expected given the target removal of low-frequency variance. These four modes reduce the variance from 0.039 to 0.023, or 41%. Furthermore, subsequent LFC removals result in spatial variance in β remaining near 0.022. Removing HFC modes (Fig. 1.4i–l) reddens the SST signal across the basin but does not appear to significantly reduce spatial heterogeneity in β. Removing the first two HFCs reduces variance from 0.039 to 0.031, or 21%, and subsequent removals do not appreciably reduce the variance, in some cases increasing it (Fig. 1.4m).

1.4 Discussion

The analysis presented here suggests that there are regions with substantial differences in spectral slope estimated over 1000-year intervals due to different realizations of internal variability. This conclusion has implications for proxy interpretation and siting, as well as possible model deficiencies in their representation of low-frequency SST variability.

Among SST proxy records in the North Atlantic Ocean, we find systematically higher values in the 10- to 100-year spectral slope β relative to the CESM Last Millennium Ensemble spread

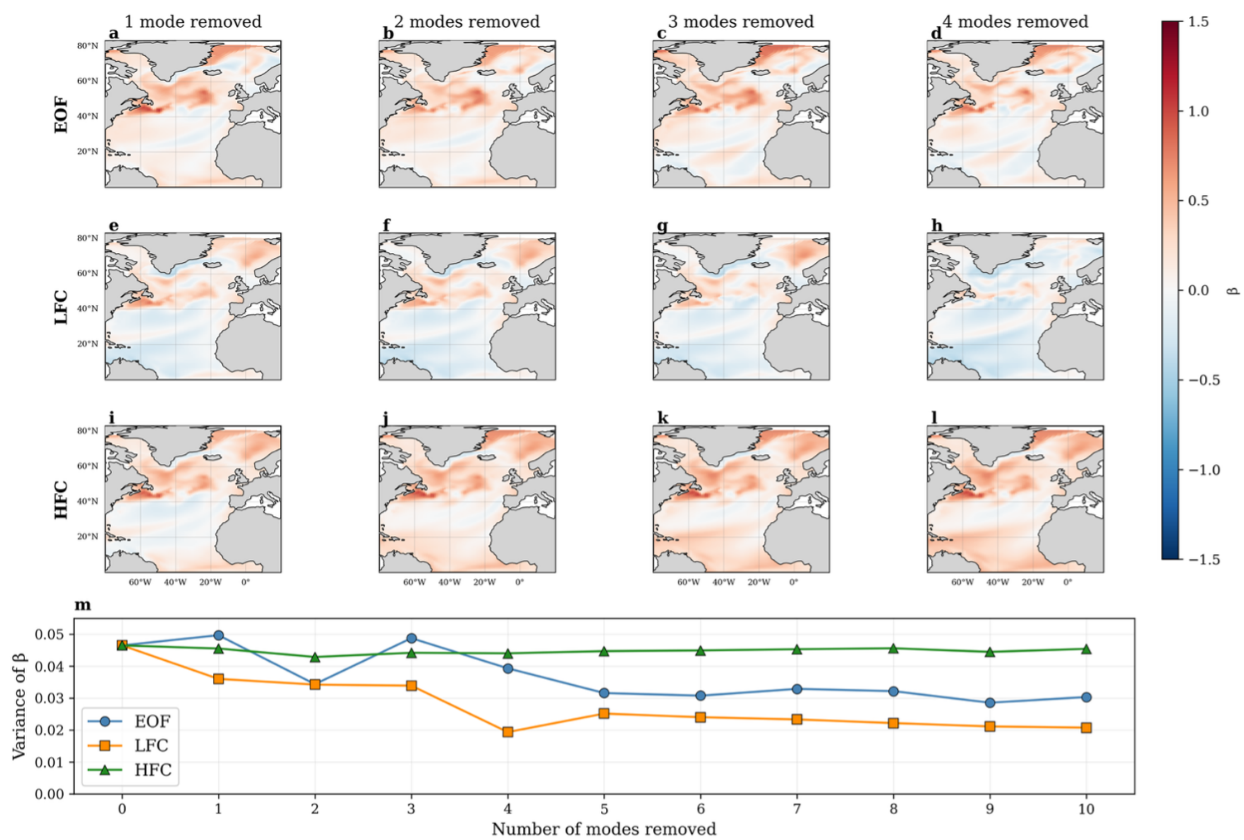

Figure 1.4: (a–h) Maps of β after iteratively removing the first four of each mode type from the model output. (m) Variance in β remaining in the North Atlantic after each mode removal.

(Fig. 1.1c), indicating that the ratio of low- to high-frequency variance is larger in the proxy records than the model simulations. While the canonical values of β in the ocean range from 0 to 2 (*Huybers and Curry*, 2006), proxies in this study showed β as high as 3.7. Several factors could lead to this disagreement. For instance, if a proxy is recording SST in a low-pass filtered fashion, such as reflecting subsurface temperature, it could overrepresent the low-frequency variability relative to the high-frequency. Proxies are also collected from high sedimentation regions in order to obtain high temporal resolution, and such regions are located in coastal areas and therefore may not fully represent temperature elsewhere in the 1-degree grid cell from the LME. In addition, climate models are known to underrepresent low-frequency variability (*Laepple and Huybers*, 2014). The proxies also display little agreement among each other in β, despite being collected from nearby areas. Notably, the model ensemble also shows significant spread between β values at nearby points. Therefore, rather than investigating the model-proxy disagreement directly, our study focuses on the spatial spread in β and the dynamics that can influence it to inform how exactly the model-proxy disparity should be interpreted in light of internal variability.

The Low Frequency Component Analysis reveals leading modes of variability in the North Atlantic for frequencies below $1/50$ yr^{-1} from the LME output that strongly highlight regions of deep water formation in the Labrador and GIN Seas (Fig. 1.3e–h), as well as parts of the Gulf Stream Extension, indicating regions in which atmospheric forcing is integrated over long periods of time in the ocean. This stands in contrast to the EOFs and high frequency patterns from the region, which highlight more variability in the subtropics. The SPG and GINS regions are also highlighted as regions of anomalously high β for their respective latitudes, seen in both the LME data (Fig. 1.2) as well as in other studies (e.g., *Huybers and Curry*, 2006).

Mode removal experiments (Fig. 1.4) demonstrate that the LFC modes explain an outsized fraction of spatial heterogeneity in β (44% of variance explained by first 4 modes) as compared to the EOF (13%) and HFC (18%) modes, despite the hypothesis that isolating higher-frequency modes may explain spatial variance more effectively. The LFC removals also decrease variance in a mostly monotonic fashion, while removing EOFs and HFCs iteratively can add variance into the spatial distribution of β. This highlights the nonlinear nature of the spectral slope, as it is a regression in logarithmic space to a squared linear operator, i.e. the Fourier transform. Nevertheless, the relative monotonicity of variance reduction in β from LFC removals reflects the well-suitedness of LFCA to explain β and indicates that the variability in SST in the SPG and GINS may, in fact, be a first-order control in the spatial heterogeneity of temperature spectra within the North Atlantic Ocean. While the LFCs cannot definitively explain either the full spatial variance in β or the model-proxy mismatch, the ability of corresponding Low Frequency Patterns (LFPs) of SST variability in the SPG and GINS to explain a large portion of spatial variance in β suggests that constraining internal variability in this region within models is a necessary precondition to reconciling the proxies with the model. The LFPs can also point to regions with temperature spectra that are most indicative of the basin mean; for example, proxies 3 and 4, which were taken off the northwest coast of Scotland, are in an area with low magnitude in all LFPs and show values of β close to the model output. Conversely, proxies located in areas of high magnitude in the leading LFPs are subject to strong internal variability influencing β. Proxy records 1, 7, 8, 9, 10, and 11 are located in such areas, and show substantial disagreements with the model spread. However, other proxies (5, 6) taken from the low LFP-magnitude areas disagree with the model, and therefore the LFCs do not tell the complete story.

This chapter establishes a method for diagnosing drivers of spatial heterogeneity in the spectral slope β using Low-Frequency Component Analysis and other orthogonal mode decompositions. We find that low-frequency SST variability in areas of deep water formation, i.e. the GIN Seas and North Atlantic Subpolar Gyre, can account for 44% of spatial variance in spectral slope within the North Atlantic Ocean using four leading LFC modes to reconstruct temperature, in contrast to EOF and HFC modes that explain far less spatial variance. These findings suggest that improving model representation of variability in such regions is a necessary component to improving model-proxy disagreement in spectral space, and also point to areas of low LFP magnitude as potential proxy sites with better representation of the basin-wide signal.

Chapter 2

Optimal Atmospheric Drivers of Sea Surface Temperature Variability in the Southern Ocean

This chapter was submitted to Geophysical Research Letters as Rosenberg et al. (under review).

Key Points

- We identify a wind pattern that drives interannual SST variability in the Southern Ocean more effectively than the Southern Annual Mode
- We demonstrate the explanatory power of this pattern using multiple configurations of an ocean state estimate
- Our results highlight the importance of winds in the Pacific sector for driving zonally-averaged SST variability

2.1 Introduction

Variability in Sea Surface Temperature (SST) within the Southern Ocean impacts stratification, sea ice extent (*Purich et al.*, 2021), and SST in the tropical Pacific Ocean (*Kang et al.*, 2023). SST in the region also has global implications due to the Antarctic Circumpolar Current (ACC) connecting the three primary ocean basins and the Southern Ocean's role in sequestering 20–40% of anthropogenic carbon since 1992 (*Zhong et al.*, 2024). Processes driving SST variability include the global meridional overturning circulation (MOC) (*Armour et al.*, 2016), wind-driven advection and upwelling (*Russell et al.*, 2006), sea ice formation and melt (*Haumann et al.*, 2020), and variations in surface heat flux (*Song*, 2020). In addition to interannual variations, the spatial mean SST (hereafter SST) in the Southern Ocean cooled from 1979 to 2010 as the rest of the global ocean warmed (*Dong et al.*, 2023). However, observed interannual variability of SST, including amplitudes, spatial patterns, and the sign of the cooling trend, is inconsistent with historical simulations in the Coupled Model Intercomparison Project (CMIP) (*Dong et al.*, 2023; *Wills et al.*, 2022).

Interannual atmospheric variability in the Southern Hemisphere is dominated by the Southern Annular Mode (SAM, *Gong and Wang*, 1999; *Marshall*, 2003). The SAM index is defined by the difference in zonal mean sea level pressure between 40°S and 65°S, and is correlated with a zonal band of westerly wind near the ACC (*Gong and Wang*, 1999). The SAM has been implicated in driving SST variability within the Southern Ocean through both heat and momentum fluxes (*Kostov et al.*, 2017). A positive SAM was observed for most of the satellite record beginning in 1979 in response to depletion of the ozone layer in the Southern Hemisphere (*Ferreira et al.*, 2015), roughly corresponding to the same time period as the observed SST cooling (*Thompson et al.*, 2011). This coincident timing suggests a link between positive SAM and SST cooling, which is consistent with Ekman transport of cold water near the continent equatorward into the rest of the Southern Ocean due to enhanced westerlies (*Ferreira et al.*, 2015). However, while the SAM trend and the seasonal relationship between SST and SAM are both well represented in CMIP models, the interannual SST trend is not, as only a weak correlation persists between the two on interannual timescales (*Dong et al.*, 2023). This model evidence suggests that trends in SAM may not be the dominant driver of the observed SST cooling. The question of what drives the observed SST trend, as well as variability on shorter time scales, remains open.

Previous investigations have examined drivers of interannual SST variability via statistical relationships (e.g., regression, *Dong et al.*, 2023) or from forward modeling experiments using imposed atmospheric forcing to calculate variations in a particular quantity of interest (e.g., factorial experiments, *Haumann et al.*, 2020). Here, we instead use the adjoint of an ocean model (the MITgcm) to derive optimal drivers using SST as our quantity of interest. The adjoint calculates the sensitivity of SST to changes in surface fluxes, obtained by algorithmic differentiation of ocean model code. Previous work has used adjoint modeling to attribute observed ocean variability to surface processes in studies of sea ice concentration (*Fukumori et al.*, 2015), mode water formation in the Southern Ocean (*Pimm et al.*, 2024), and ACC strength (*Mazloff*, 2012). The model adjoint takes as an argument the scalar SST, which is expressed as a weighted sum of ocean state variables over a specified time period. The adjoint returns the sensitivity $\partial \mathrm{SST}/\partial \phi(\tau)$, where ϕ is the vector of control variables (zonal and meridional components of wind stress, net heat flux, etc.) at each grid point and τ is the temporal lag prior to the evaluation of SST. The adjoint sensitivity allows examination of the linearized response of an ocean quantity to perturbations of external forcing.

Adjoint sensitivities can also be used to derive modes of variability in atmospheric fluxes that are optimized to drive variations in SST using Dynamics-weighted Principal Component Analysis (DPCA, *Amrhein et al.*, 2024). DPCA identifies modes (Dynamic Principal Components, DPCs) that are orthogonal in time. Each of the DPCA modes is associated with a spatial pattern (Empirical-Dynamical Function, EDF). Unlike Empirical Orthogonal Functions (EOFs, *Lorenz*, 1956), the EDF patterns are not orthogonal in space. The DPCA method has been used to study drivers of variability of heat content in the North Atlantic Subpolar Gyre (*Amrhein et al.*, 2024) and the strength of the Atlantic Meridional Overturning Circulation (AMOC, *Stephenson et al.*, 2024). In *Stephenson et al.* (2024), forward ocean model simulations driven by the derived DPCs demonstrate ocean dynamical pathways that mediate changes in AMOC. Wind stresses found in this study were dissimilar from traditional atmospheric modes, illustrating the ability of DPCA to identify novel drivers of ocean variability. By contrast, in *Amrhein et al.* (2024), heat flux DPCs are qualitatively similar to the canonical index of the North Atlantic Oscillation, which is the dominant mode of variability in the region, demonstrating that the method can also recover known results.

Here we use DPCA to find optimal patterns of atmospheric variability that drive interannual SST variability in the Southern Ocean in the Estimating the Circulation and Climate of the Ocean Version 4, release 4 state estimate (ECCO, *Forget et al.*, 2015), a forced ocean model simulation using the Massachusetts Institute of Technology general circulation model (MITgcm, *Marshall et al.*, 1997; *Adcroft et al.*, 2004). We evaluate the variance in SST explained by the derived patterns, as well as that of the SAM, through a set of forward modeling experiments.

2.2 Methods

We use the forward and adjoint versions of the MITgcm as packaged through ECCO Modeling Utilities (EMU), a free-to-use software package. EMU is based on analyses performed in *Fukumori et al.* (2021), in which adjoint sensitivities were used to explain the physical drivers of Beaufort Gyre sea level rise by modeling sensitivity to changes in freshwater in the region. EMU uses a global, nominal 1-degree version of the MITgcm with 50 vertical levels and parameterizations for the effects of vertical mixing (*Gaspar et al.*, 1990) and mesoscale eddies (*Redi*, 1982). EMU contains the compiled solution to the ECCO version 4, release 4 product (*Forget et al.*, 2015). ECCO, in turn, is an exact forward solution to the MITgcm in a forced ocean and sea ice configuration, with atmospheric forcing, initial conditions, and mixing parameters adjusted to fit the ocean state to observations in the period 1992–2017. Because the state estimation is performed by adjusting external forcing, and not adjusting the model state itself, the solution obeys model physics and contains closed budgets for volume, mass, and tracers in the ocean interior, thereby maintaining causal relationships between surface drivers and interior ocean variability. The adjoint model in EMU is compiled via Transformation of Algorithms in Fortran (TAF, *Giering et al.*, 2005). For this study we define our quantity of interest, SST, as the area-weighted mean SST between 48°S and 61°S (Fig. 2.1) averaged over the last year of the ECCO simulation (January 1–December 31, 2017).

We use the flux-forced and atmospheric state-forced configurations of the MITgcm (*Adcroft et al.*, 2004; *Marshall et al.*, 1997), hereafter "FF" and "SF," respectively. In FF, wind stress and fluxes of heat and salt are prescribed at 6-hour intervals, whereas in the SF, the surface air temperature, humidity, and wind speed are prescribed and fluxes are derived using bulk formulae. EMU computes sensitivities based on a FF version of ECCO. Since fluxes in the FF version of ECCO are computed using the outputs of the bulk formulae in the SF version, output from the two versions is identical to within machine precision. However, the distinction between SF and FF becomes important when interpreting adjoint sensitivities and running forward simulations with adjusted forcing, as feedbacks to the atmosphere are absent from FF, which in some cases can lead to drift in the ocean state (e.g., *Kostov et al.*, 2019) relative to SF. In addition, wind stress is specified independently of the heat fluxes in FF so changes to wind stress do not affect heat flux. Fluxes of heat, salt, and momentum due to sea ice are preserved in FF using the modeled sea ice parameters from ECCO. Here we use EMU to derive optimal forcing patterns in the FF version of the MITgcm and then run additional experiments in a SF configuration to evaluate results in the presence of a full sea ice model and atmospheric feedbacks.

To compute the DPCA, we begin by constructing a matrix $\mathbf{S}$ of sensitivities of SST to heat flux, where the columns of $\mathbf{S}$ represent spatial points at the ocean surface and the rows represent lags. We similarly calculate a matrix of sensitivities to zonal and meridional wind stress, concatenated in the spatial dimension so that EDFs are patterns of vector winds. We approximate $\mathbf{S}$ to be stationary;

i.e., that the sensitivity to a variable at a certain point and lag does not meaningfully change with the time at which SST is calculated, and we assume that the fluxes can be represented as white noise processes (i.e., uncorrelated in time), as in *Hasselmann* (1976). Next, we construct matrices $\mathbf{X}$ of heat flux and wind stress anomalies from ECCO, with rows indexing time and columns spatial points. The DPCA is then found from the singular value decomposition of the matrix $\mathbf{X}^T\mathbf{S}$, and the forcing patterns are found by projecting the left singular vectors onto the data matrix $\mathbf{X}$. We refer to the left singular vectors as Dynamic Principal Components (DPCs) and their regression onto the data matrix as Empirical-Dynamical Functions (EDFs). The DPCs and EDFs are ordered by their contributions to SST variance. A complete description of the method can be found in *Amrhein et al.* (2024) and *Stephenson et al.* (2024).

In addition to EDFs, we compute leading Empirical Orthogonal Functions (EOFs, *Lorenz*, 1956) and Stochastic Optimals (SOs, *Farrell and Ioannou*, 1996; *Kleeman and Moore*, 1997) of both heat flux and wind stress. These can be interpreted as the dominant patterns of atmospheric variability ("what the atmosphere does") and of adjoint sensitivities ("what the ocean wants"), respectively. EOFs and SOs are computed as the left singular vectors of the $\mathbf{X}$ and $\mathbf{S}$ matrices defined above, respectively. To eliminate high-frequency variability dominating on 6-hour time scales that is unlikely to be important for driving SST, we apply a first-order, 1-year, low-pass Butterworth filter on $\mathbf{X}$ before computing EOFs.

2.3 Results

2.3.1 Linear decomposition of atmosphere-ocean fluxes

EOF, SO, and EDF analyses of heat flux and wind stress yield leading candidate patterns for driving ocean variability that differ qualitatively. The leading EOF of heat flux (Fig. 2.1a) represents 40% of interannual variance in ECCO heat fluxes, with large amplitudes near the Amundsen Sea Low

(ASL), which lies in the Pacific sector between 60°S and 70°S. The leading EOF of wind stress (Fig. 2.1d) explains 50% of the variance of the ECCO wind stress south of 20°S and is similarly strongest in both magnitude and curl in the ASL, with reduced amplitude in the Indian and Atlantic sectors relative to the Pacific.

The SOs are patterns of surface fluxes that optimally perturb SST based solely on model physics; i.e. what the ocean "wants" the atmosphere to do in order to increase SST variance. The leading heat flux SO (Fig. 2.1b) is nearly uniform over the entire region where SST is averaged and explains over 90% of the adjoint sensitivity, indicating an efficient role for local heating. The leading wind stress SO (Fig. 2.1e) explains over 60% of the sensitivity and has a thin zonal band of westward wind stress anomalies directly over the northern boundary of the averaging region. This pattern corresponds to southward Ekman transport at the northern boundary of the domain and in other regions that align with bathymetry and coastal geometry to flux heat anomalies into the averaging region.

Finally, we turn to the EDFs, which combine information from model physics and historical flux variability to derive atmospheric patterns that drive ocean variability. The leading EDF of heat flux accounts for 90% of the variance of SST due to heat flux (Fig. 2.1j). The heat flux in the leading EDF pattern is positive everywhere within the ACC, with strongest magnitude to the southeast of New Zealand (Fig. 2.1c). The wind stress EDF accounts for 75% of the SST variance due to wind stress (Fig. 2.1f) and is predominantly eastward over the ACC with largest amplitudes in the Indian and Pacific sectors and a large wind stress curl near the ASL. The EDFs can be thought of as a middle ground between the EOFs and SOs, whereby regional susceptibilities of the ocean to hypothetical fluxes are reconciled with actual atmospheric activity. A characteristic of the EDFs (Fig. 2.1h–j) is their spectral steepness relative to that of the EOFs, indicating that a subset of atmospheric features can be implicated in driving the ocean.

As an additional comparison, we compute the SAM index following the definition of *Gong and Wang* (1999) as the difference in zonal mean sea level pressure between 40°S and 65°S, using

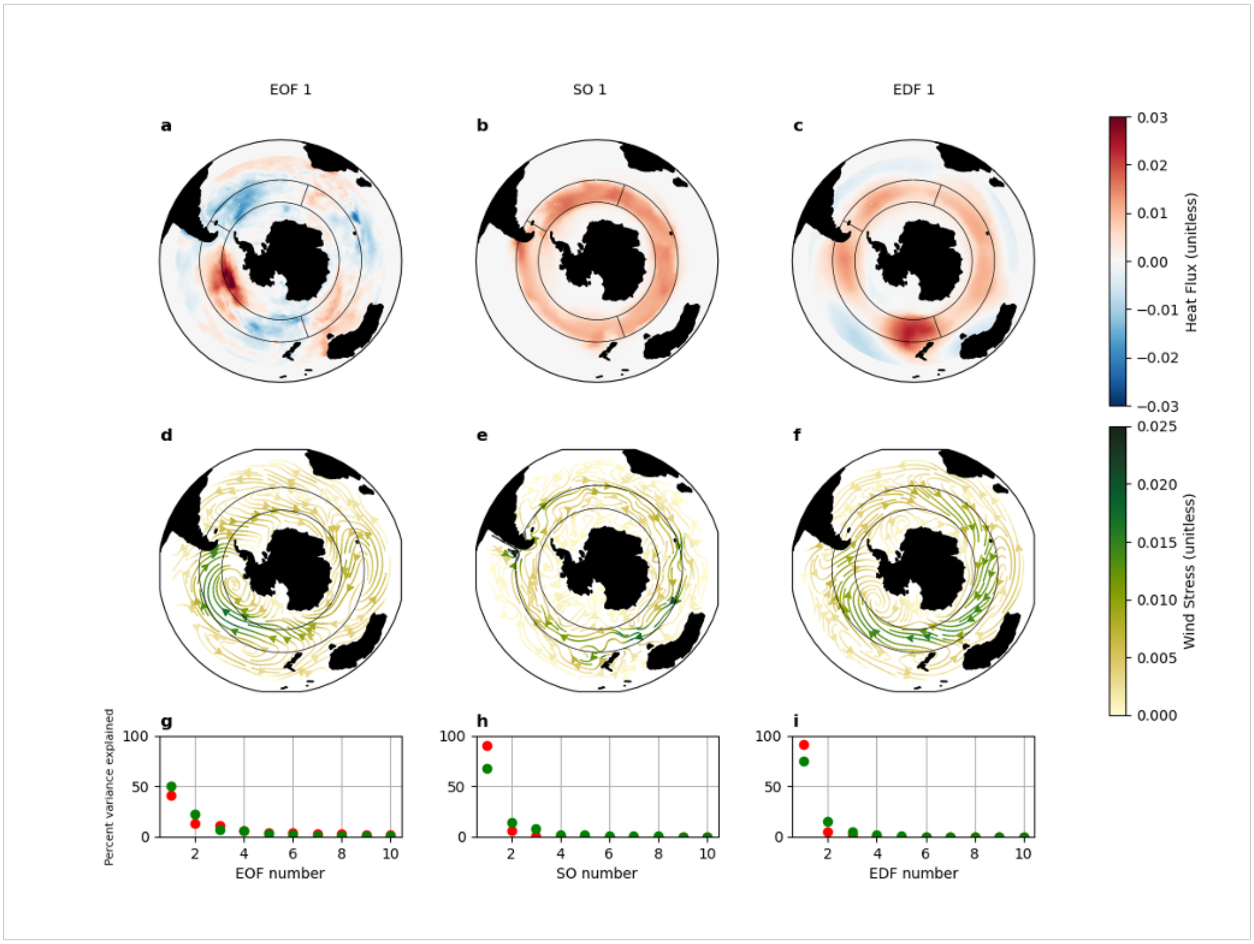

Figure 2.1: (a–f) Leading EOFs (left), SOs (center), and EDFs (right) of heat flux (a–c) and wind stress (d–f). Black lines at 61°S and 48°S show the horizontal extent of the domain over which SST is defined for adjoint sensitivity calculations. (h–j) Spectra describing the percent variance accounted for by leading modes of each decomposition method (wind stress in green, heat flux in red).

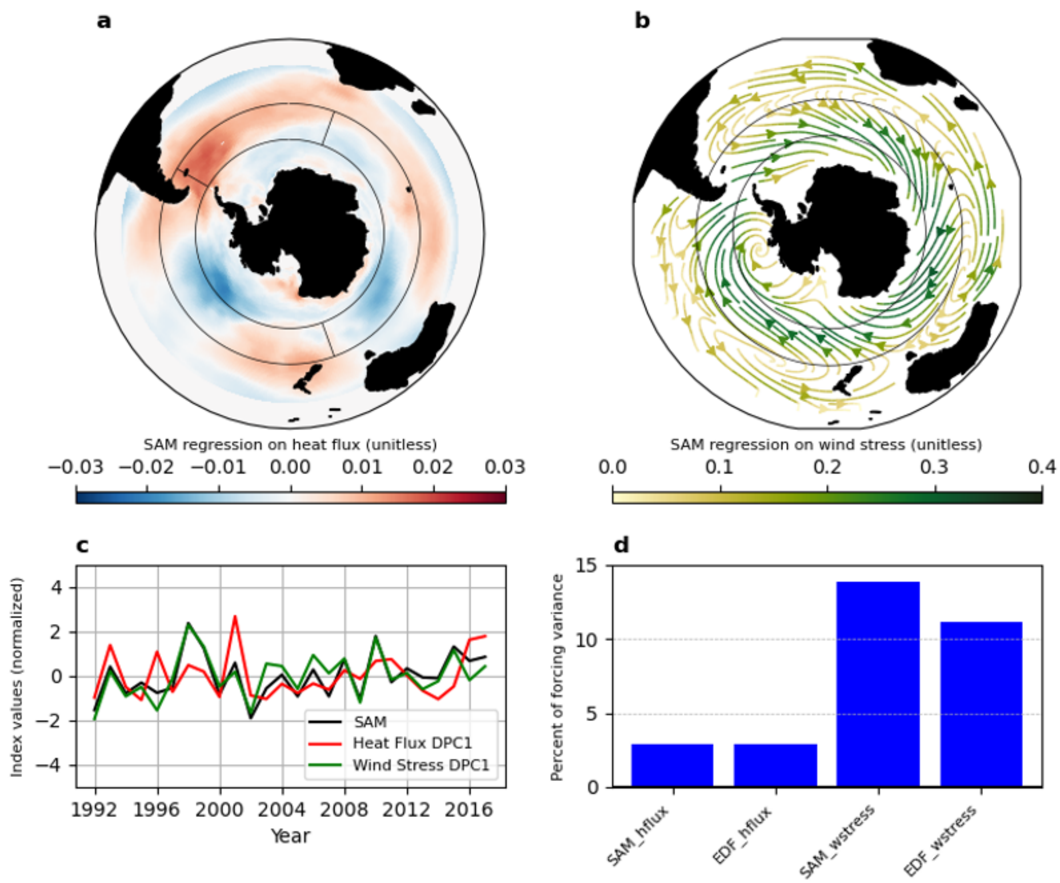

Figure 2.2: (a–b) Maps of ECCO heat flux (a) and wind stress (b) regressed onto the SAM index, as defined by *Gong and Wang* (1999). (c) Annual averaged leading dynamic principal components (DPCs) of heat flux and wind stress, as well as the normalized SAM index. (d) Fraction of interannual atmospheric forcing anomalies south of 20°S explained by each pattern.

ECCO sea level fields. We calculate the regression pattern for each variable as the inner product of the SAM time series with the flux anomaly matrix $\mathbf{X}$. The leading DPC time series of wind stress is correlated with the SAM index ($r^2 = 0.56$) (Fig. 2.2c); however, there are qualitative differences in their corresponding spatial patterns. The regression pattern of SAM on wind stress (Fig. 2.2b) is approximately zonally symmetric with eastward wind stress anomalies at a maximum over the ACC, whereas the EDF of wind stress is zonally asymmetric and shows a relatively lower magnitude of wind stress in the Atlantic (Fig. 2.1f). The leading DPC of heat flux, by contrast, shows no correlation with the SAM and exhibits less interannual variation (Fig. 2.2c). The heat flux EDF (Fig. 2.1c) is more zonally symmetric than the regression of SAM onto heat flux (Fig. 2.2a). It is worth noting that the SAM accounts for more of the total interannual variance in both heat flux and wind stress within the domain than do the DPCs (Fig. 2.2d), illustrating the greater efficiency of the DPC in driving SST in the linearized system.

2.3.2 Evaluation in a nonlinear model

The leading EDF patterns for both wind stress and heat flux explain a large majority of the variance in the SST under the assumption (made when using adjoint sensitivities) that SST responds linearly to atmospheric fluxes in the MITgcm. To evaluate the role of EDFs in a nonlinear model under finite-amplitude perturbations, we rerun the ECCO state estimate with EDF and SAM variability regressed out of forcing variables, and investigate changes in SST variance relative to that found in ECCO. We first perform three forward model simulations in the FF model with the following modifications to the forcing field: (1) the first EDF of heat flux is removed (“EDF_hflux”), (2) the first EDF of wind stress is removed (“EDF_wstress”), and (3) both the heat flux and wind stress EDFs are removed simultaneously (“EDF_both”). We perform similar experiments using SAM-related wind stress and heat flux (“SAM_hflux,” “SAM_wstress,” “SAM_both”).

EDF_hflux results in a 6.9% reduction in interannual variance of the SST relative to ECCO while EDF_wstress results in a 68.5% reduction in the variance (Fig. 2.3c). When both EDFs are removed simultaneously, the variance is reduced by 82.9%. Thus the responses of the contributions from individual forcing components do not add linearly. We attribute this result to constructive contributions from correlated heat flux and wind stress. By contrast, removing SAM_hflux results in an 8% increase in SST variance while removing SAM_wstress results in a 38.6% reduction, and SAM_both results in a 42.3% reduction. In all of the SAM experiments, the ocean retains much of the interannual variability in SST (Fig. 2.3a), and year-to-year fluctuations such as the large temperature decrease in 2000 remain. Evidently, fluxes correlated with SAM are not as effective in reducing the variance as are the EDFs.

For purposes of diagnosing trends in SST, we are limited by the coverage period of ECCO, which begins in 1992, while the canonical trend begins in 1979 (*Armour et al.*, 2016; *Dong et al.*, 2023; *Ferreira et al.*, 2015). Nevertheless, we examine the possible role of EDFs in driving trends over the ECCO period, during which the ECCO state estimate shows a 0.1 K/decade cooling trend in SST (Fig. 2.3b). Removing the heat flux and wind stress EDFs from the forcing reduces the cooling trend to 0.07 and 0.03 K/decade, respectively, and removing both components results in a slight warming of 0.0008 K/decade. In contrast, removing the heat flux, wind stress, and both components of the SAM from the forcing result in cooling trends of 0.10, 0.07, and 0.07 K/decade, respectively. Thus the combination of heat flux and wind stress EDFs can explain the SST cooling trend from 1992 to 2010 while associated SAM fluxes do not.

Sea ice variability plays major roles in mediating fluxes in the Southern Ocean (*Ferreira et al.*, 2015) that is not represented in the FF model. Turbulent air-sea feedbacks, e.g., on heat fluxes due to changing ocean temperatures, are also not represented. To assess the robustness of our results in the presence of feedbacks and dynamic sea ice, we repeat variance attribution experiments in the SF configuration. We regress the heat flux DPC (“EDF1_hflux_state”), wind stress DPC (“EDF1_wstress_state”), and SAM index (“SAM_state”) out of the ECCO atmospheric state forcing, including winds, temperature, humidity, precipitation, pressure, and shortwave and longwave radiation. Fluxes of heat, momentum, and fresh water between the atmosphere, sea

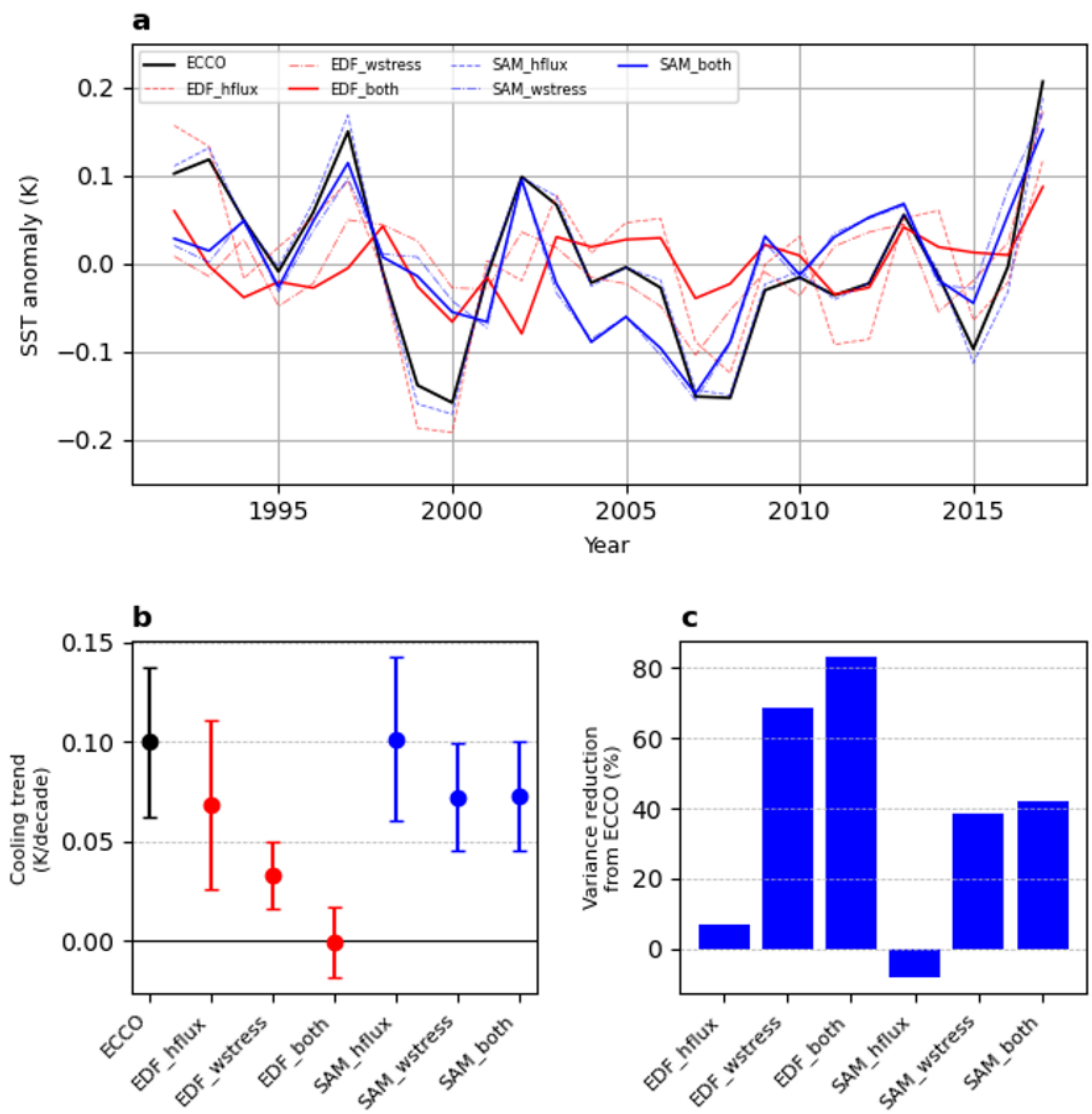

Figure 2.3: (a) Annually-averaged SST from ECCO (black) as well as in EDF-DPC removal experiments (red) and SAM removal experiments (blue) in the MITgcm. (b) SST cooling trends in ECCO and flux removal experiments from 1992–2010. Error bars represent standard error from the linear fit. (c) Interannual SST variance removed in forcing removal experiments compared to ECCO. Larger values indicate lower variance as compared to ECCO.

ice, and ocean are then computed via bulk formulae within the MITgcm from the prescribed atmosphere and simulated sea ice and ocean. In this case, EDF1_hflux_state results in a 9.7% reduction in interannual variance and EDF1_wstress_state results in a 38.2% reduction, whereas SAM_state results in a 23.8% reduction (Fig. 2.4b). EDF1_wstress_state reduces the cooling trend in SST to 0.074 K/decade, while the trends in EDF1_hflux_state and SAM_state are 0.092 and 0.093 K/decade, respectively. Thus, while we relied on the FF configuration to compute leading EDFs, those structures are more effective than the SAM even in the SF model. The possible roles of sea ice and turbulent feedbacks in reducing the imprint of major modes of interannual variability on the SST trend from 1992–2010 are a subject of future study.

2.4 Discussion

By leveraging an ocean model adjoint in conjunction with the DPCA method, we identify one heat flux pattern and one wind stress pattern which, when combined, explain 83% of interannual variance in the Southern Ocean spatially-averaged SST in the flux-forced ECCO ocean state estimate. These patterns are derived by combining information about ocean physics and historical atmospheric variability. The modes found using DPCA comprise slightly less of the total interannual variance in heat flux and wind stress than does the SAM; however, they account for substantially more variance in the SST on interannual timescales than the SAM. Within the time period available for analysis, the patterns we find explain the SST cooling trend in a flux-forced model, unlike the SAM. When evaluated in a configuration with interactive sea ice and turbulent fluxes, the leading EDFs still outperform the SAM, suggesting generalizability of modes derived in FF configurations. While the state-forced pattern removal experiments do not show as large a decline in SST variance and trend as compared to the flux-forced, we emphasize that the DPC modes are derived from sensitivities to flux variables and are not necessarily optimized for atmospheric state variables. Future work could consider computing DPCs using state sensitivities, which are not computed in

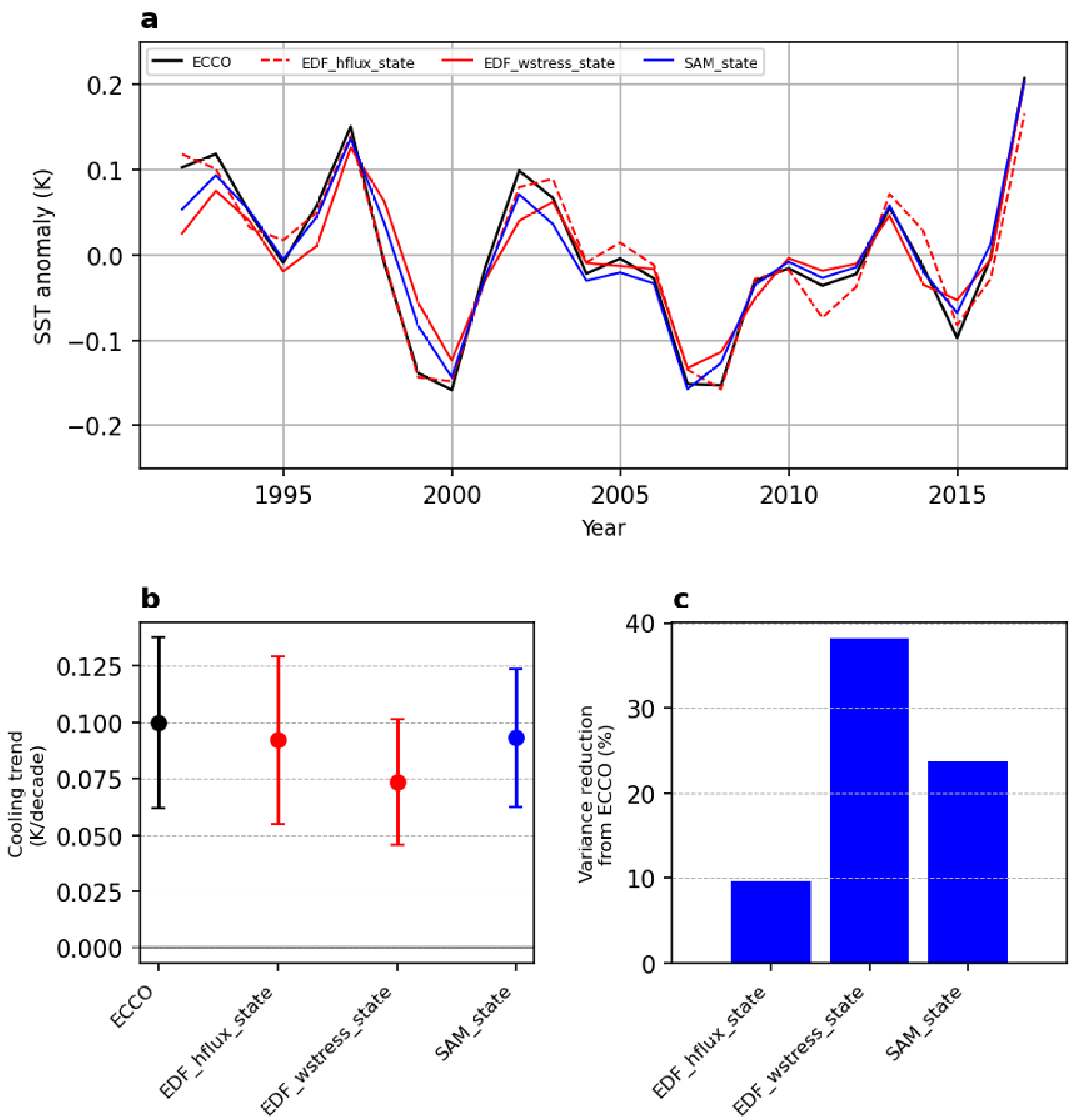

Figure 2.4: Same as Figure 2.3, but for atmospheric state-forced experiments.

EMU at present.

The spatial structure of EDFs reveals that regional atmospheric forcing plays a decisive role in driving Southern Ocean SST variability. The leading wind stress EDF, which drives SST most effectively, is markedly more zonally asymmetric than the SAM wind stress pattern, and exhibits stronger wind stress curl across most of the Southern Ocean, particularly in the Pacific basin (Fig. S1). This enhanced curl suggests that the EDF drives stronger vertical motions and heat convergence within the averaging region than the SAM, although the precise mechanisms by which the wind stress EDF controls SST warrant further investigation. The highlighted importance of the Pacific is consistent with previous work identifying the Pacific sector as the locus of significant Southern Ocean cooling (*Wills et al.*, 2022), and together these results imply that zonally asymmetric wind stress variability in the southern Pacific is more important for explaining and predicting zonal-mean Southern Ocean SST than the comparatively zonal SAM pattern. More broadly, the observed asymmetry of changes in SST and upper ocean heat content between the Pacific sector and the Atlantic and Indian sectors (*Hague et al.*, 2024; *Song et al.*, 2024), suggests that the dominant drivers of Southern Ocean SST variability are fundamentally regional in character. While the present study focuses on spatially averaged SST across the full Southern Ocean basin, the adjoint framework employed here is well suited to targeting regional drivers of variability, and extending this analysis to subregional quantities of interest is a natural direction for future work.

Chapter 3

Examining drivers of zonally asymmetric heat content variability within the Southern Ocean

Key Points

- A novel method is introduced to derive optimal atmospheric drivers of ocean variability across all forcing variables are found using an adjoint model.
- Two leading modes are defined that efficiently drive zonal asymmetry in upper 700 m temperatures in the Southern Ocean.
- The leading mode is strongest in winter and drives wind-driven advection in the Southeastern Pacific, while a second-order mode drives asymmetry year round.

3.1 Introduction

The ocean acts as an integrator of atmospheric variability by virtue of its large heat capacity and slow timescales of ocean circulation (*Hasselmann* (1976); *Gebbie* (2021); *Frankignoul and Hasselmann* (1977)). Surface fluxes of heat and momentum from the atmosphere drive anomalies in ocean temperature and circulation that persist far longer than the atmospheric forcing that generated them, producing low-frequency variability that in turn influences climate (*Hasselmann* (1976)), carbon uptake (*Frölicher et al.* (2015)), and fluxes back to the atmosphere (*Deser et al.* (2010)). A natural question therefore arises: which features in the atmosphere drive particular changes in the ocean, and by which mechanisms? Although theoretical and modeling studies have explored how the ocean responds to changes in the atmosphere, the pathways and mechanisms by which the ocean changes have largely been explored by analysis of observations or idealized forced ocean and coupled models. For instance, evaluation of correlations between atmospheric indices and ocean state variables can suggest dominant mechanisms that drive oceanic changes (e.g., *Hasselmann* (1976); *Dong et al.* (2023)), and analyses of atmospheric and ocean states during El Niño-Southern Oscillation (ENSO) and other coupled events can point to the driving role of such modes (e.g., *Karoly* (1989); *Deppenmeier et al.* (2021)). Idealized forward modeling experiments in which prescribed atmospheric anomalies are used to force ocean-only models that are diagnosed to understand oceanic processes during and following the adjustment to the applied forcing (e.g., *Ferreira et al.* (2015); *Hague et al.* (2024)). While much progress has been made using these methods, there are limits to the strength of the results. Observations can provide insight into these adjustment processes, but atmospheric drivers have rich spatial and temporal structure that makes it difficult to interpret what aspects of the atmospheric fields drive the particular quantity of intereset (QoI). Here, we take advantage of the results from a model adjoint that gives the optimal drivers of aspects of the ocean circulation and structure. The adjoint is derived by algorithmic differentiation of a forward model simulation, yielding the derivative of the resulting QoI with respect to all input variables (*Heimbach et al.* (2005)). Because the adjoint is generated from algorithmic differentiation of the model equations, this approach reveals causal, physical pathways between the model inputs and outputs (*Stephenson and Sévellec*, 2021; *Stephenson et al.*, 2024).

The Southern Ocean is the primary conduit for exchange of water properties between the Atlantic, Pacific, and Indian Ocean basins via the Antarctic Circumpolar Current (ACC), and is responsible for a disproportionate fraction of the global uptake of heat and anthropogenic carbon by the ocean (*Frölicher et al.* (2015); *Talley et al.* (2011)). Observations have revealed interannual cooling in the upper ocean over recent decades, a trend at odds with the global pattern of anthropogenic warming and one that is not found in historical simulations in coupled climate models (**?***Kostov et al.* (2017); *Wills et al.* (2022)). Recent work has highlighted, however, that this zonal-mean cooling occurs in the presence of substantial inter-basin asymmetry. The Pacific sector and the Atlantic–Indian sector of the Southern Ocean exhibit out-of-phase variability in upper ocean heat content on interannual to decadal timescales (*Hague et al.* (2024); *Roemmich et al.* (2015); *Wang et al.* (2021)), with the Pacific sector dominating zonal-mean variations and driving much of the apparent cooling signal since 1979 (*Hague et al.* (2024); *Roemmich et al.* (2015); *Wang et al.* (2021); *Wills et al.* (2022)). Therefore, indices of temperature asymmetry within the basin may be a more natural focus of investigation into interannual variability than a basin-mean approach. This asymmetry can also be found in observed air-sea fluxes of anthropogenic carbon dioxide (*Prend et al.* (2022)). Factorial modeling studies, in which one forcing variable is isolated at a time (*Hague et al.* (2024)), and observational analyses (*Song et al.* (2025); *Ni et al.* (2026)) find that wind stress changes associated with the Interdecadal Pacific Oscillation (IPO) and ENSO are the dominant driver of the observed asymmetry, particularly within the ACC region (approximately between 48°S 61°S). These atmospheric teleconnections modulate the strength and position of the Southern Ocean westerly wind belt (*Li and England* (2020)), driving convergence and divergence of oceanic meridional heat transport that produce the out-of-phase temperature response between basins. The Amundsen Sea Low (ASL, *Turner et al.* (2013)), a climatological atmospheric low typically located within the Bellingshausen and Amundsen Seas, modulates wind strength and wind stress curl in the Pacific sector. The ASL has also been connected to temperature asymmetry (*Ni et al.* (2026)). While ENSO weakly correlates with the ASL strength and position, these quantities are also driven at higher frequencies by storm tracks originating in the midlatitudes (*Raphael et al.* (2016)), indicating that higher frequency atmospheric variability than associated with the IPO and ENSO may also drive some of the observed changes.

Here, we examine the PmAI, defined in *Song et al.* (2024) as the difference between the upper 700 meter vertically-averaged temperature between the Pacific and Atlantic–Indian sectors of the Southern Ocean. We employ Dynamics-weighted Principal Component Analysis (DPCA, *Amrhein et al.* (2024)) to examine optimal atmospheric drivers of the Southern Ocean temperature asymmetry as measured by PmAI.

This chapter extends the DPCA framework introduced in Chapter 2 in two important respects. First, rather than deriving optimal forcing patterns of a single atmospheric variable (i.e., heat flux or wind stress), we derive modes that account for all forcing variables simultaneously. Thus we are able to investigate the ocean response to coherent modes of co-varying atmospheric fluxes, rather than to individual atmospheric fields acting independently. This also allows us to investigate oceanic impacts of the optimal atmospheric driving patterns using the state-forced model. This contrasts with the flux-forced simulations used in Chapter 2. To construct a common basis across variables with different physical units, we multiply each atmospheric flux by its corresponding local adjoint sensitivity before performing the DPCA decomposition. The resulting sensitivity-weighted flux anomalies represent the contribution of each forcing element to changes in the PmAI index, providing a natural normalization that places all variables in units of the index itself. The resulting Dynamic Principal Components (DPCs) represent the multivariate atmospheric patterns that most efficiently drive variability in inter-basin temperature asymmetry, weighted by the ocean's sensitivity to each forcing.

After identifying the leading DPCA patterns, we conduct a series of targeted perturbation experiments. In these simulations, individual modes are applied as perturbations to the model forcing for a single month. Using a heat budget, we quantify the oceanic dynamical pathways by which each atmospheric mode drives inter-basin asymmetry, and we investigate the seasonality of the response of the ocean to each mode. We find two modes that reconstruct most of the variance in the PmAI index: a leading-order mode that drives temperature changes in the Pacific sector of the Southern Ocean but not the Atlantic-Indian sector, and a second-order mode that drives roughly equal and opposite temperature responses in the Pacific and Atlantic-Indian sectors. Changes in the southeast Pacific are driven by wind-driven advection, and these changes explain the bulk of decadal variability in the asymmetry. Changes in winds in the southwest Pacific and the strength of westerlies in the Atlantic-Indian sector explain a smaller fraction of variations in the PmAI index.

3.2 Adjoint Results

We use the adjoint model as packaged in ECCO Modeling Utilities (EMU) described in *Fukumori et al.* (2021). We first define an objective function that represents the PmAI index (*Song et al.* (2024)): the volume-averaged temperature in the upper 700m of the Pacific sector of the Southern Ocean (60°W to 20°E, 61°S to 48°S), minus the volume-averaged temperature in the upper 700m in the Atlantic-Indian sector (20°E to 60°W, 61°S to 48°S). The adjoint results presented here are calculated targeting the PmAI index in December 2017, which is the final month of the ECCO simulation that was used in *Fukumori et al.* (2021). To assess the seasonal dependence of the adjoint sensitivities, we also run the adjoint model for July 2017 (not shown) and find that the sensitivities are very similar to those in December 2017; therefore, we use December 2017 sensitivities throughout the calculations described below.

In order to validate the adjoint sensitivities, we perform a linear reconstruction of the PmAI index over the entire model simulation period (1992-2017) using only the adjoint sensitivities and atmospheric fluxes (Figure 1a, orange line) following *Fukumori et al.* (2021). We compare this to the index computed directly from the ECCO temperature field (orange line in fig. 1a). The reconstruction gives an estimate of the temporal evolution of the index δJ_i due to a single forcing variable $\boldsymbol{\phi}_i$ at time t by convolving the adjoint sensitivities $\frac{\partial J}{\partial \boldsymbol{phi}}$ with atmospheric fluxes $\boldsymbol{\phi}_i$:

$$\delta J_i(t) = \sum_{\tau} \sum_{\mathbf{r}} \frac{\partial J}{\partial \boldsymbol{\phi}_i(\mathbf{r}, \tau)} \boldsymbol{\phi}_i(\mathbf{r}, t - \tau), \tag{3.1}$$

where $\mathbf{r}$ represents horizontal points at the ocean surface and τ is the lag in weeks prior to time t. The full index J is computed by summing equation 3.1 over all forcing variables i. This includes the net heat flux, shortwave heat flux, zonal and meridional wind stress, fresh water flux, surface salt flux due to sea ice formation and melt, subsurface salt plume flux due to sea ice, and sea level pressure. The convolution using unadjusted adjoint gradients displays an unrealistic seasonality in the PmAI reconstruction due to the contributions of net heat flux. To correct this, we use only the interannual component of the sensitivity to heat flux by applying a 52-week boxcar filter to the adjoint gradients before computing the convolution, following *Fukumori et al.* (2021). The full adjoint sensitivities, with the adjusted heat flux sensitivities, are able to reconstruct 72% of the variance in the PmAI index as determined by the r^2 value calculated between the true index and the reconstruction (eq. 3.1). Thus 72% of the monthly PmAI index can be explained by the reconstruction using linear sensitivities, indicating that the linear approximation is valid to first-order when investigating this quantity. Most of the variance in the reconstructed index comes from the contributions of net heat flux and zonal wind stress (fig. 3.1a, gold and dark blue lines).

3.3 Compound DPCA

From the adjoint output, we construct adjoint sensitivity matrices $\mathbf{S}_i = \frac{\partial J}{\partial \boldsymbol{\phi}_i(\mathbf{r}, \tau)}$, where $\boldsymbol{\phi}_i$ represents the various atmospheric variables, with dimensions of horizontal spatial points ($\mathbf{r}$) by weekly time lags (τ). As in Chapter 2, we next construct matrices $\mathbf{X}_i$ of the 6-hourly atmospheric flux anomalies used to drive the forward flux-forced model where i represent the different forcing variables. We construct a matrix $\mathbf{C}$ that has dimensions of time by lag, and contains the spatial covariances between the sensitivities and flux anomalies across all variables,

$$\mathbf{C} = \sum_i \mathbf{X}_i^T \mathbf{S}_i. \tag{3.2}$$

Note that while $\mathbf{S}_i$ and $\mathbf{X}_i$ generally have different units for different atmospheric forcing variables i, their products all have units of °C, and therefore the summation is well-defined. This allows us to examine optimal modes of atmospheric variability driving the ocean which may exist across multiple atmospheric variables (e.g., correlated heat and momentum fluxes). This results in larger spatial covariances between adjoint sensitivities and forcing anomalies in the matrix $\mathbf{C}$ than what would be found by calculating only across a single forcing variable. We decompose $\mathbf{C}$ into left and right singular vectors:

$$\mathbf{C} = \mathbf{U}\mathbf{\Xi}\mathbf{V}^{\mathbf{T}}, \tag{3.3}$$

where the rows of $\mathbf{U}$ are termed Dynamical Principal Components (DPCs), $\mathbf{\Xi}$ is a diagonal matrix containing the singular values ξ_i, and the rows of $\mathbf{V}$ are termed Sensitivity Principal Components (SPCs). The DPCs are time series with the same time step as the flux anomalies $\mathbf{X}$, and the SPCs are lag series with the same lag spacing as the adjoint sensitivities $\mathbf{S}$.

If the time step in $\mathbf{X}$ and the lag spacing in $\mathbf{S}$ are equal, we can express the convolution in equation 3.1 at time t_k in terms of the data matrices as:

$$J(t_k) = \sum_{i=1}^{k} \mathbf{C}_{k-i+1,i} \tag{3.4}$$

The elements of $\mathbf{C}$ can be expressed in terms of the DPCs, SPCs, and singular values:

$$\mathbf{C}_{ij} = \sum_m \xi_m \mathbf{U}_{i,m} (\mathbf{V}^T)_{m,j} \tag{3.5}$$

where m indexes over the columns of $\mathbf{U}$. Thus, the i, j element of $\mathbf{C}$ is the singular value-weighted sum of the ith component of every DPC multiplied by the jth component of every SPC. Then, the full convolution time series (3.4) assumes the simple form:

$$J = \sum_m \xi_m(\text{DPC}_m * \text{SPC}_m) \tag{3.6}$$

where $*$ represents the standard discrete convolution operator for finite sequences, truncated by the length of the time dimension. In practice, given 6-hourly flux anomalies and weekly sensitivities, we first take weekly averages of the DPC before performing the convolution. In the limit where only one singular value is significant, the full reconstruction (eq. 3.1) can be approximated using only the leading DPC-SPC pair:

$$J \approx \xi_1(\text{DPC}_1 * \text{SPC}_1). \tag{3.7}$$

Using this methodology, we can estimate the contribution of each DPC-SPC pair to the PmAI at every time step, as well as its contribution to the total PmAI variance.

We find two leading DPC-SPC pairs that account for the majority (74%) of the variance in the PmAI index using equation 3.6, and are correlated to the QoI ($r^2 = 0.77$). This value is slightly larger than the 72% from the full adjoint sensitivities (section 3.2). The variance explained by the DPC-SPC is *greater* than fact that the variance explained by the full adjoint is possibly due to spurious correlation introduced by temporally smoothing out the high-frequency features in the full reconstruction (compare orange line in fig. 3.1a to 3.1b). The convolution of DPC1 and SPC1 is significantly correlated with the total QoI ($r^2 = 0.57$, $p < 0.01$) and accounts for 45% of the variance. The reconstruction from DPC1 qualitatively mirrors the decadal oscillations seen in the ECCO PmAI time series (compare blue and black lines in Figure 3.1b), whereas the convolution of DPC 2 and SPC 2, which accounts for 21% of the PmAI variance ($r^2 = 0.28$) may explain some of the higher-frequency features such as the decrease in 1996 (red line, fig. 3.1b). However, the limited number of realizations of decadal variability (~2.5) prevents us from a more quantitative evaluation of variance explained as a function of frequency band. We also examine the Niño-3.4 index and the IPO Tripole index (TPI, *Henley et al.* (2015)) using SST from ECCO, and find that while DPC 1 is qualitatively similar to the IPO and Niño 3.4 (fig. 3.1e), the r^2 values computed between DPC 1 and the indices are only 0.18 and 0.13, respectively, indicating that the variance in DPC 1 is not the same as either of these indices. In addition, DPC 2 does not correlate with either index ($r^2 = 0.1$ and 0.07, respectively) (fig. 3.1f).

We use Empirical-Dynamical Function (EDF) by regressing the leading DPC time series onto the flux anomaly data matrices $\mathbf{X}_i$. The DPCs are calculated across all flux variables (section 3.3) and thus the EDFs are multivariate. EDF 1 (fig. 3.2) has strong cyclonic wind stress near the northern part of Bellingshausen Sea with magnitude close to the spatial-mean standard deviation of wind stress anomalies and a band of zonal wind stress of similar magnitude south of Australia and New Zealand. The Bellingshausen Sea wind stress is strong in the region of the climatological position of the Amundsen Sea Low in Austral summer (*Fogt et al.* (2012); *Turner et al.* (2013)). EDF 1 also an area of high sea level pressure (SLP) in the regression onto sea level pressure near the Bellingshausen Sea, with smaller values elsewhere. The net heat flux pattern shows modest amplitudes south of New Zealand and near the ASL. It reaches up to half of a standard deviation of the flux anomalies that drive ECCO south of New Zealand and near the ASL. Freshwater flux and shortwave flux do not show strong patterns do not exhibit strong magnitudes in their EDF components. Significant features in surface and subsurface salt fluxes due to sea ice are confined to coastal regions off Antarctica.

EDF 2 (fig. 3.3) is stronger in the Atlantic-Indian basin for all variables than EDF 1. The wind stress is strong and cyclonic in a region closer to the climatological position of ASL in Austral winter than found in EDF 1, and has a zonal band of easterly anomalies that extends throughout the Atlantic-Indian sector. The cyclonic pattern in the Pacific is qualitatively similar to regions where the IPO plays a role in controlling the winds via atmospheric teleconnections (*Yu et al.* (2024)). However, EDF2 winds are not correlated with the IPO as noted above. The net heat flux component

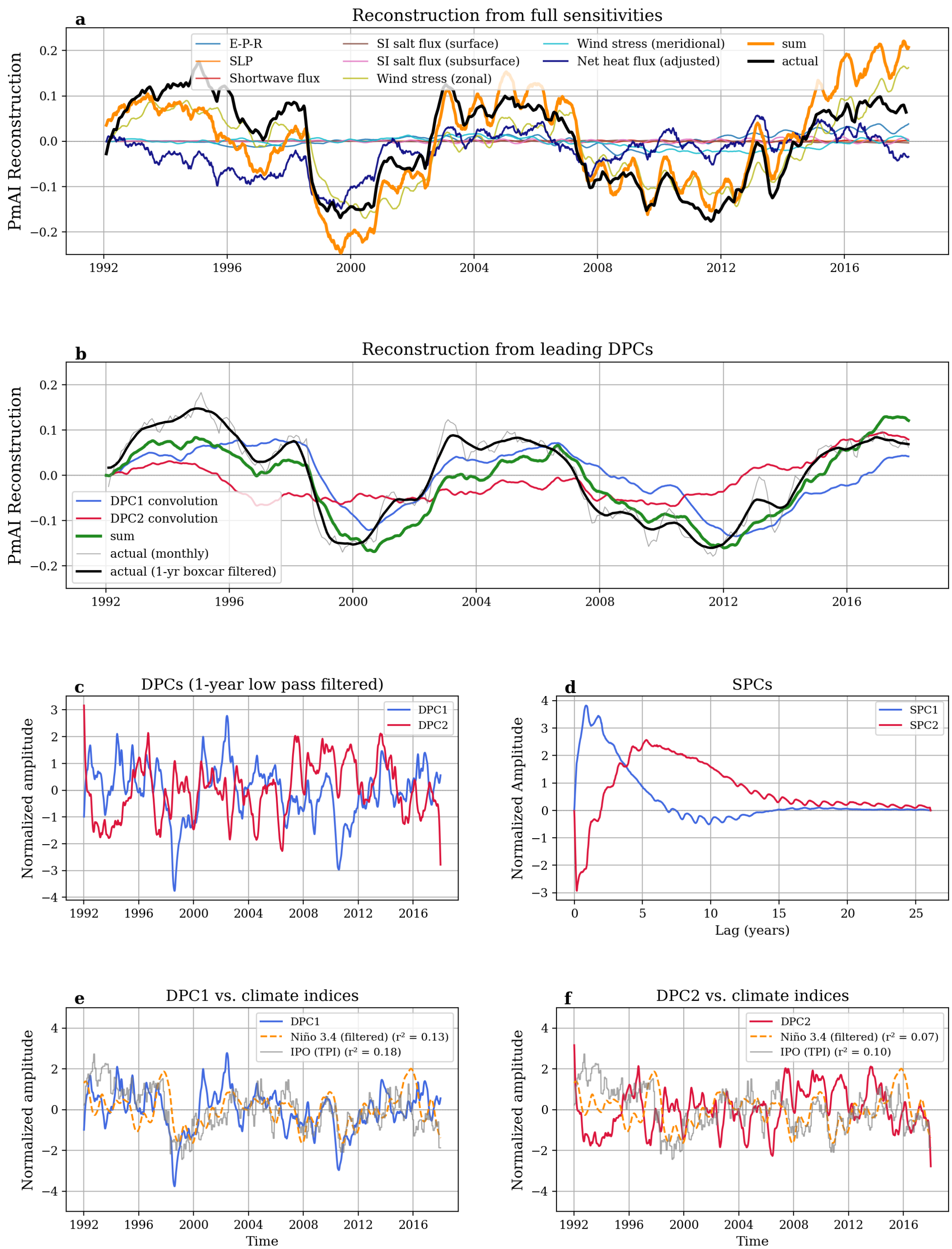

Figure 3.1: (a) Reconstructions (eq. 3.1) of PmAI index computed using full adjoint sensitivities for each forcing variable, as well as their sum (gold) and the full QoI time series from ECCO (black). (b) Reconstruction approximated by leading two DPC-SPC pairs (eq. 3.6), with 1-year boxcar averaged QoI time series plotted in black. (c,d) Leading DPCs (c) and SPCs (d), defined by eq. 3.3. (e,f) Comparison of leading DPCs with 1-year filtered Niño 3.4 and unfiltered IPO Tripolar index.

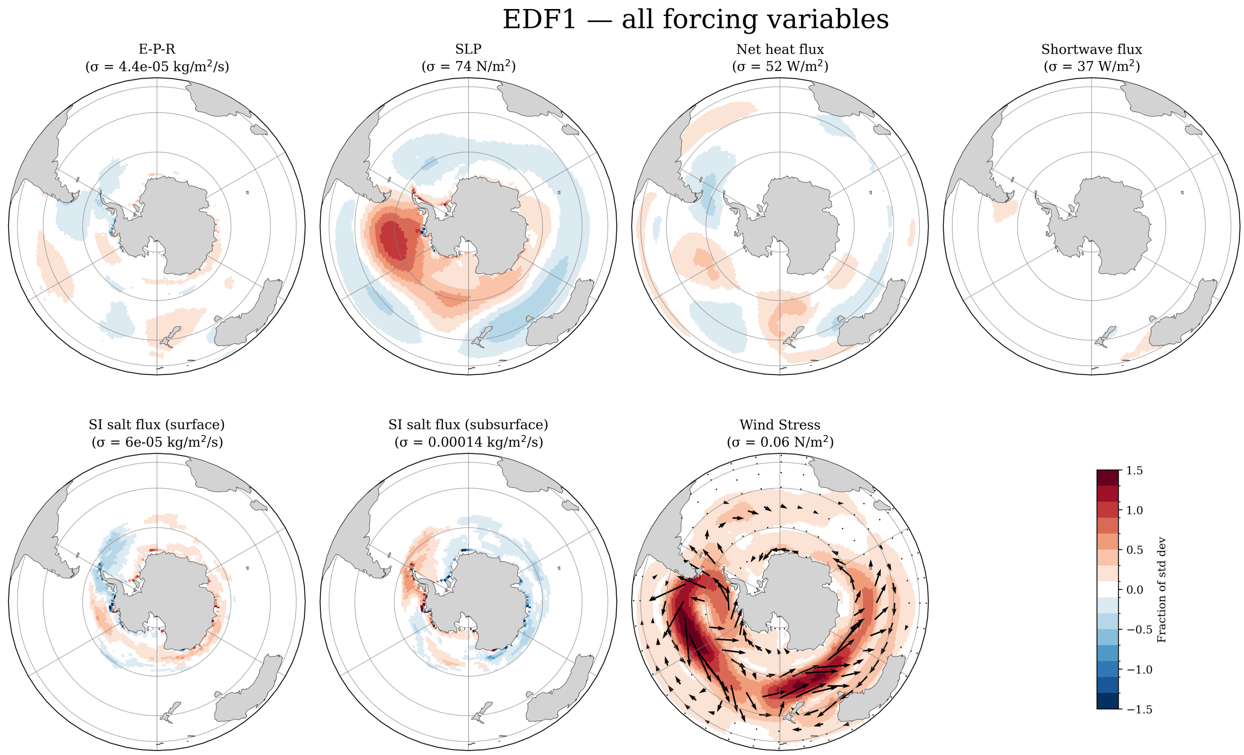

Figure 3.2: EDF 1 computed across all flux variables. From top left: Fresh water flux, sea level pressure, net heat flux, shortwave flux, surface salt flux due to sea ice, subsurface salt plume flux, and wind stress. Values are shown as a fraction of the spatial-mean standard deviation of flux anomalies for each variable.

of EDF2 has moderate negative values that are on the order of 10 W/m^2 near the regions of strong wind stress. As found in EDF1, EDF2 salt fluxes due to sea ice are concentrated poleward of the averaging region. The SLP component is correlated with both of the leading DPCs; however, SLP is only used in the forcing for the flux-forced MITgcm to determine the inverse barometer correction to sea surface height, and therefore does not play a dynamical role.

3.4 Forcing Removal Experiments

Equation (3.6) describes the contribution of individual DPC-SPC pairs to the full PmAI index given the linear gradient returned from the adjoin. However, the impact of the forcing patterns on the ocean is, in general, a nonlinear function given by the full model physics. In order to assess their

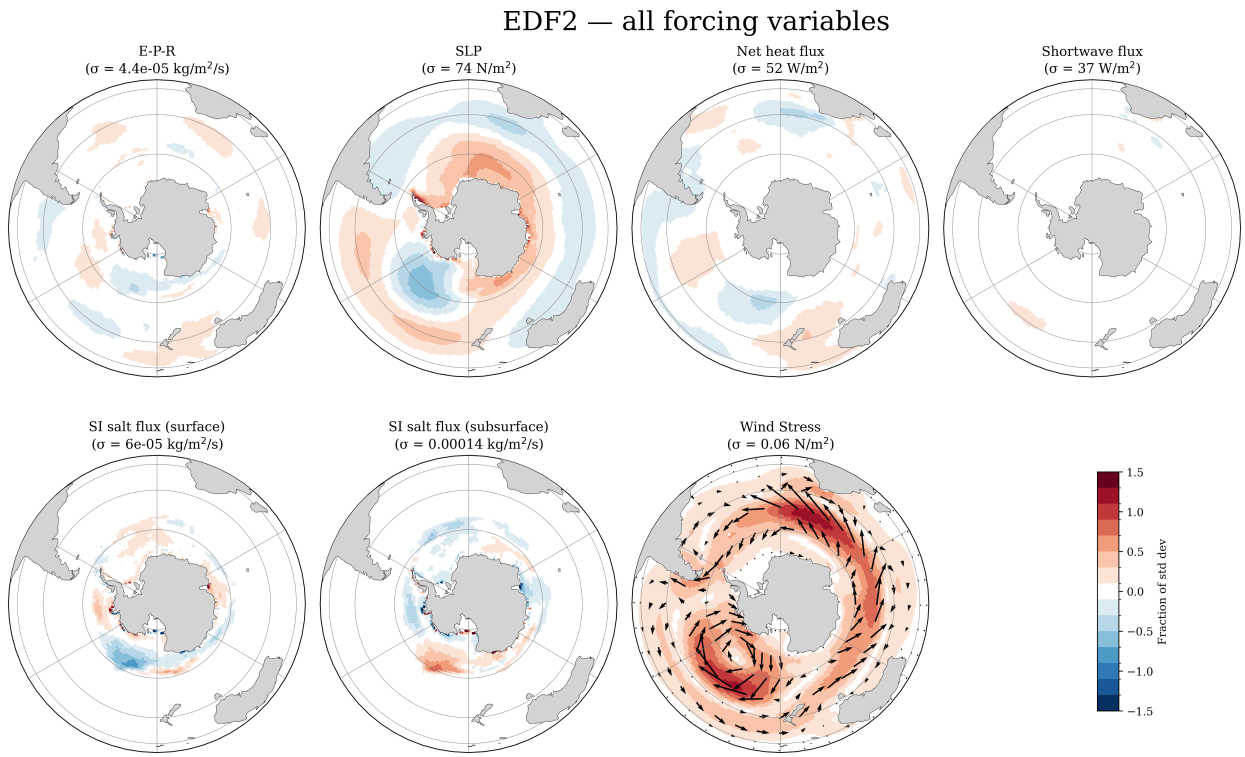

Figure 3.3: As in fig. 3.2, but for EDF 2.

full contribution to PmAI variance, we run forcing removal experiments (see *Methods*, chapter 2). We then rerun the forward model, and evaluate PmAI within the adjusted model simulation. Following this, we regress both leading DPCs out of the forcing variables at the same time in order to determine to what extent their impacts are additive and what role nonlinearities play.

The results of the forcing removal experiments are shown in figure 3.4. Removing EDF 1 (i.e., regressing out DPC 1) reduces variance in the PmAI index in the full forward model by 52% . The linear approximation (eq. 3.6), in contrast, predicts a 57% reduction. Likewise, removing EDF 2 reduces the variance by 23% while the linear results predicts 27%. When both modes are removed and the model is run again, the variance by is reduced by 69%. This likely occurs because the EDF patterns are not constrained to be orthogonal in space *Amrhein et al.* (2024), and their impacts may interact nonlinearly within the full numerical model. We also expect the EDFs in the full model to account for less variance in the PmAI index than their corresponding linear predictions (eq.

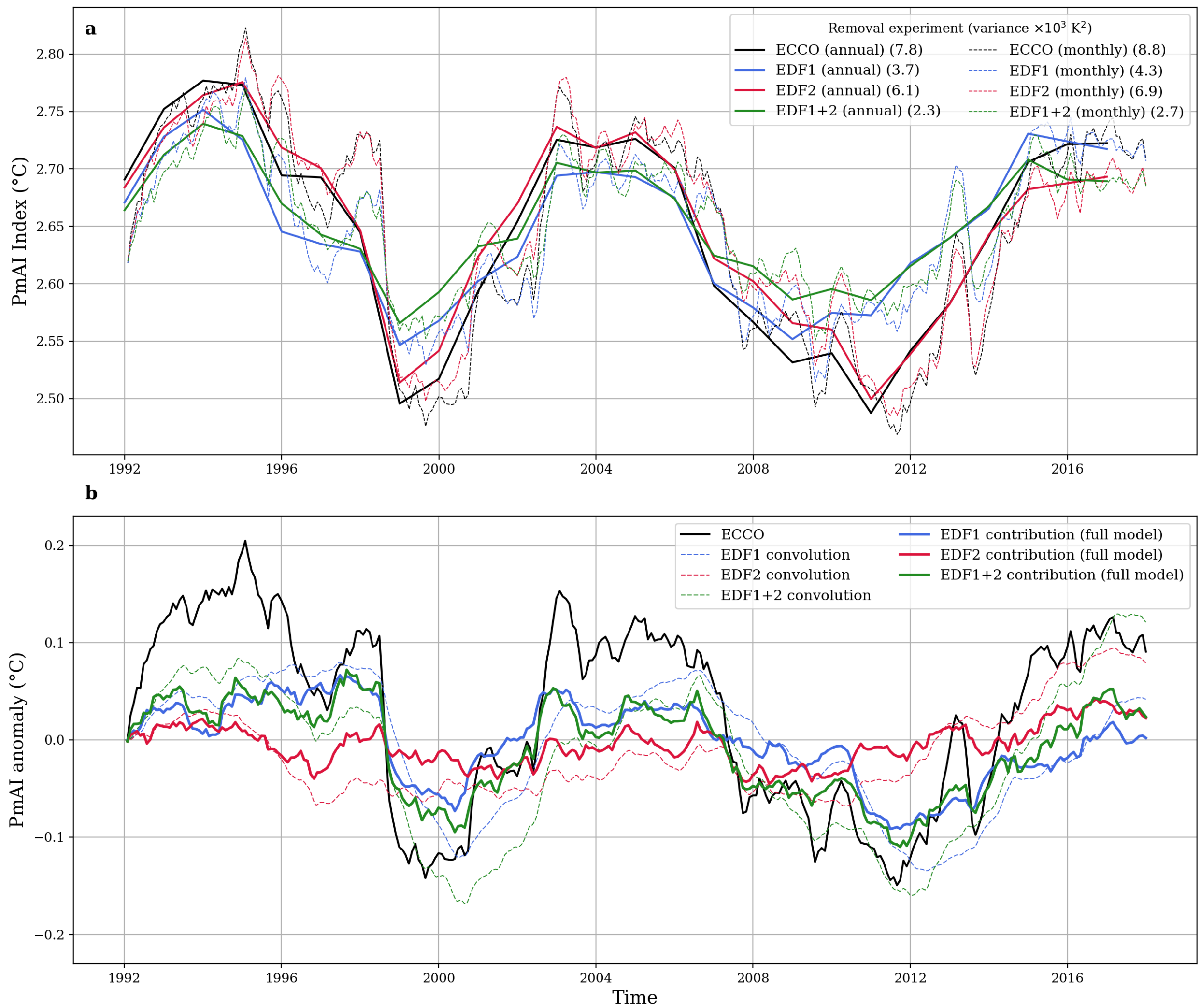

Figure 3.4: (a) QoI calculated from model output after removing leading 2 EDFs individually (blue, red) and simultaneously (green) from the atmospheric forcing. Solid lines show annual averages while dashed lines are monthly values. Variance of each time series in $K^2 \times 10^{-3}$ is shown in the legend. (b) PmAI anomaly time series explained by each EDF, calculated by subtracting each time series in part (a) from the ECCO values. Dashed lines show the linear reconstruction as in fig. 3.1b.

3.6), due to the presence of feedbacks and nonlinearities in the model. Nevertheless, the similarity between the linear convolution and full model simulations validates the assumption that the system is approximately linear in its response to the EDFs, and approaches the limit of possible explained variance in the PmAI index from the adjoint sensitivities (72%, see section 3.2). To calculate the contributions of each of the EDFs to the PmAI index (fig. 3.4b) we first remove the mean from of the PmAI index time series. We then subtract the outer product of the EDF and DPC from the forcing fields that are used to drive the ECCO product. We compare these resulting time series to the predictions from the DPC-SPC convolutions (eq. 3.6), and we find each of the EDF contribution time series to be correlated at the 99% significance level with its corresponding convolution time series: the Pearson correlation coefficient of EDF 1 is 0.88, of EDF 2 is 0.85, and of their sum is 0.88. As in the convolution (fig. 1b), EDF 2 qualitatively explains some features in the PmAI time series, such as the decrease in 1996, which isnot captured by EDF 1.

3.5 Ocean Responses to Optimal Forcings

In the previous section, we established that the leading two EDFs, which are the atmospheric patterns that are designed to optimally drive PmAI variability, are able to explain most of the PmAI variance in full, non-linear forward simulations. To determine the mechanisms by which the ocean responds to the dominant patterns can be inferred neither directly from the EDFs themselves nor from the removal experiments. EDF 1, which appears to account for the quasi-decadal oscillation in the PmAI index, has a wind stress pattern that is cyclonic and is located north of the Bellingshausen sea (fig. 3.2a). This suggests that the oceanic response occurs from of EDF1 results from Ekman pumping and suction. The impact of EDF 2 is smaller and more localized. Its impact is focused in the Atlantic and Indian Basins where westerlies likely impact the meridional Ekman transport of cold water northward from the Antarctic continental margin, but a more careful treatment is required to establish the exact pathways of temperature change.

In order to investigate these mechanisms, we run forward perturbation experiments. We take each leading EDF and scale it by 1/100 of its magnitude, and add this perturbation to the ECCO forcing for one month. We apply the perturbation in separate experiments to July 1992 and January 1993 to investigate the seasonality in the ocean's response to the atmospheric forcing. For EDF 2, we also scale the pattern by -1, as this produces a positive PmAI perturbation in the Pacific which allows for easier comparison; as the EDFs are only deterministic up to sign, this adjustment does not affect the analysis. We then subtract the ECCO temperature from the new forward model output to isolate the impact of the EDF perturbations. We assess the mechanisms of ocean response by decomposing the temperature response into constituent budget terms:

$$\frac{D\theta}{Dt} = \frac{1}{\rho c_p}(\mathcal{F}_{\text{adv}} + \mathcal{F}_{\text{diff}} + \mathcal{F}_{\text{surf}}), \tag{3.8}$$

where the left-hand side of equation 3.8 represents the point-wise trend in potential temperature, the terms on the right-hand side represent heat fluxes due to advection, diffusion, and surface fluxes, respectively, ρ is the average density, and c_p is the average specific heat capacity of seawater.

Figure 3.5 a-b shows the budget terms from ECCO in each basin with the seasonal cycle removed. The total temperature tendency is higher in the Pacific sector ($\sigma = 4.6 \times 10^{-9}$ °C/s) than the Atlantic-Indian ($\sigma = 2.4 \times 10^{-9}$ °C/s). Some of this can be attributed to the fact that advective and surface fluxes are correlated and operate in tandem in the Pacific sector (r = 0.32), in contrast to the Atlantic-Indian (r = -0.04). We also calculate the response of each budget term to each EDF perturbation experiment by subtracting out the ECCO budget terms (fig. 3.5 c-j).

The temperature response to EDF1 (1×10^{-8} °C/s) in the Pacific is one order of magnitude larger than that in the Atlantic-Indian sector ($1 - 1.5 \times 10^{-9}$ °C/s), in keeping with the overall zonal structure of wind stress in EDF 1 (fig. 3.2). The response to EDF1 is rather seasonal. The average temperature anomaly in the Pacific decays by 50% in six months following a perturbation in January. The initial response is driven by advection into the Pacific sector, while the decay

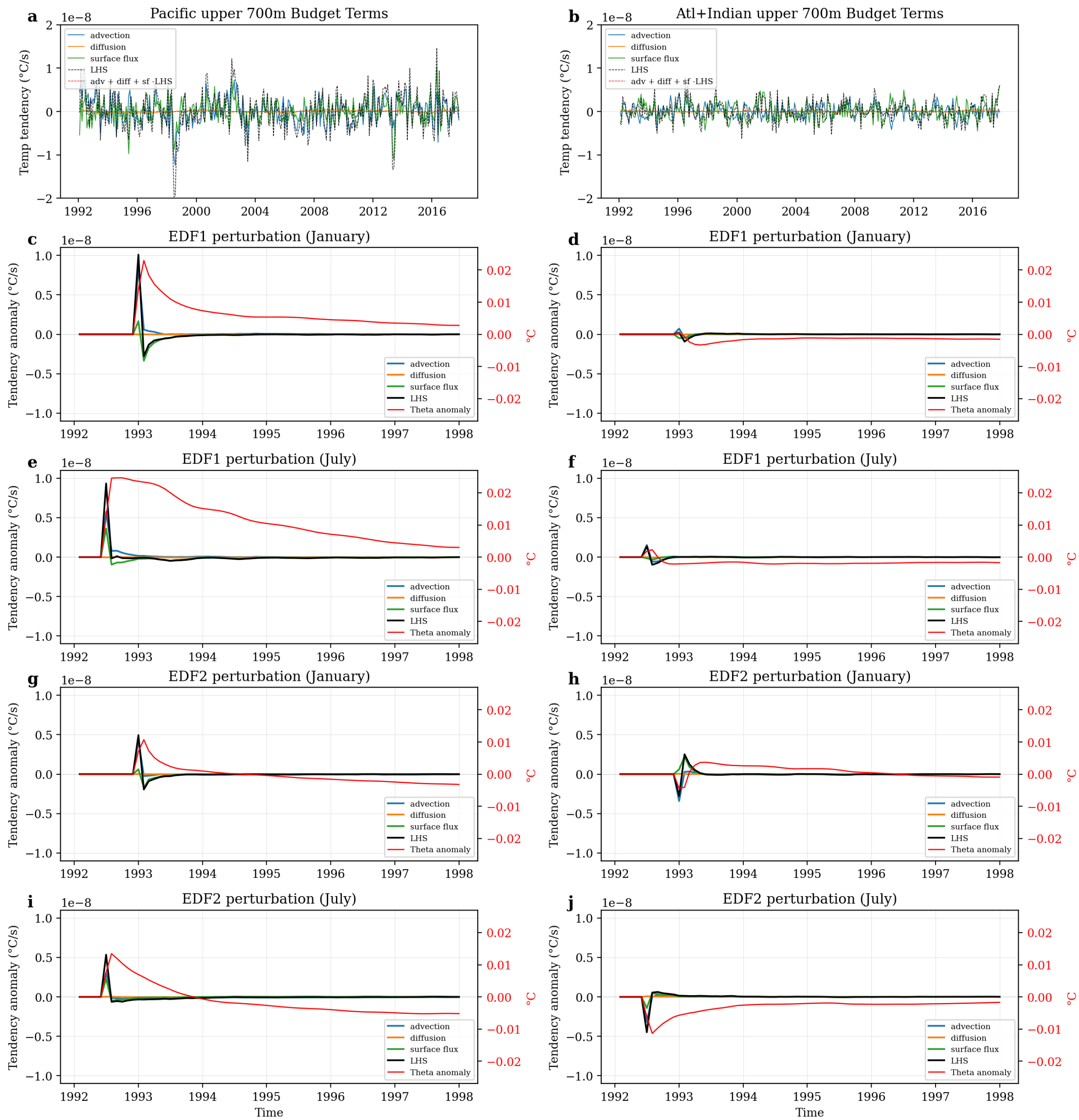

Figure 3.5: (a,b): Calculated budget terms from ECCO for upper 700m temperature in Pacific and Atlantic + Indian sectors of the Southern Ocean, respectively, with seasonal cycle removed. LHS denotes the left hand side of eq. 3.8, i.e. the diagnosed temperature tendency. (c,d): Differences in budget terms between experiment with EDF1 perturbation applied in January 1993 and ECCO, with temperature difference in red. (e,f): Same as (c,d) but for experiment with EDF1 applied in July 1992. (g-j): Same as (c-f), but for EDF2 perturbation experiments.

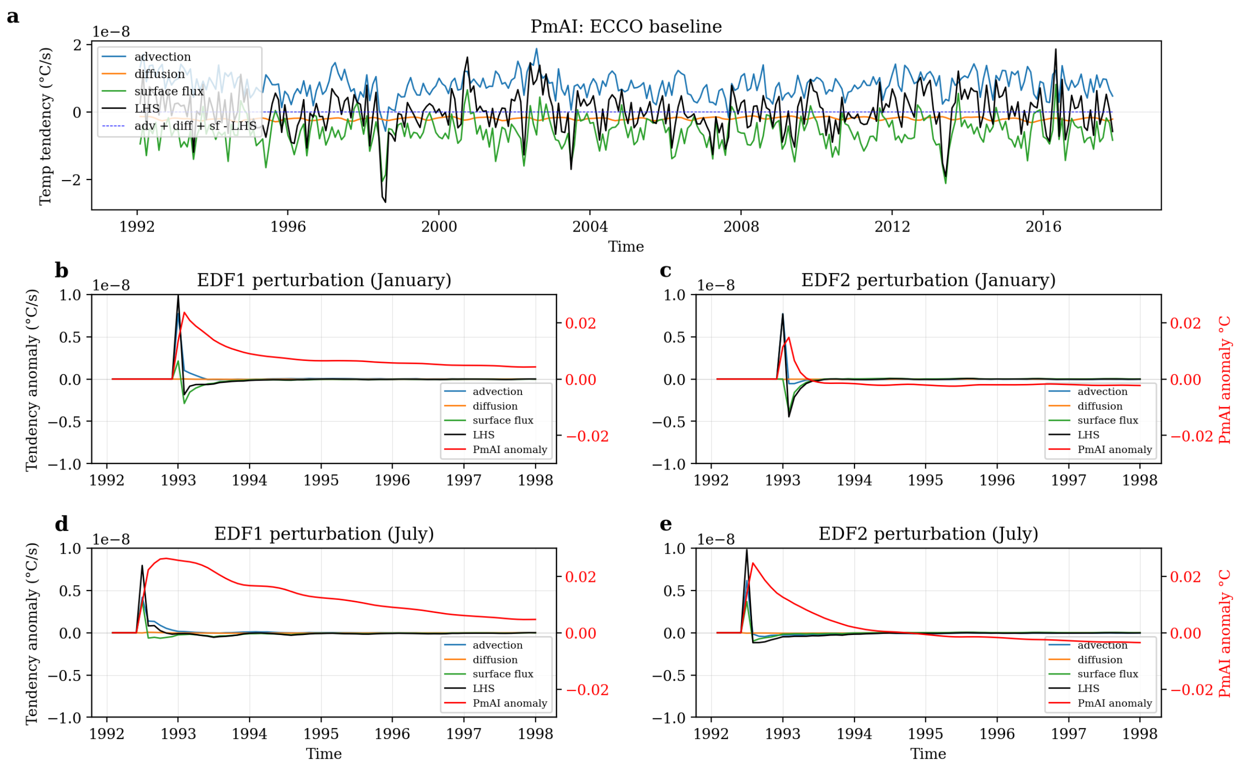

Figure 3.6: (a) Differences in ECCO between budget terms for top 700m temperature in the Pacific and the Atlantic-Indian basins. (b,d) Budget terms as in (a) subtracted from similar terms in EDF1 perturbation experiments applied in January 1993 and July 1992, respectively. (c,e) Same as (b,d), but for EDF2 perturbation experiments.

is driven by a compensating negative tendency due to surface fluxes following the perturbation. In contrast, the initial perturbation persists far longer following a July perturbation, decaying to 50% after 18 months and continuing in a qualitatively linear fashion, with only modest negative tendencies due to surface fluxes. The Atlantic-Indian sector exhibits a more modest response to an EDF1-like perturbation, despite similar seasonality to the Pacific. A perturbation in January yields roughly compensatory advective and surface-forced tendencies in the month of perturbation within the Atlantic-Indian sector, followed by negative tendencies in both. The resulting negative temperature anomaly decays by 50% within a year of the perturbation, but does not recover to ECCO values afterward. Following a July perturbation, the temperature initially increases due to advection, but immediately decreases sharply from negative tendencies due to both advection and surface flux. The temperature anomaly does not decay following the July perturbation for the rest of the simulation, but remains about 0.002 °C cooler than ECCO as negative anomalies are stored in the subsurface ocean.

Applying a perturbation of the EDF 2 pattern (fig. 3.5g-j) yields temperature responses more uniform in magnitude between the Pacific and Atlantic-Indian sectors than EDF 1. Following an EDF 2-like perturbation in January, temperature decreases by 4×10^{-9} °C in the Pacific and increases by a similar amount in the Atlantic-Indian sector. In both sectors, the anomaly decays to 50% of the initial perturbed value within six months due to compensation of the initial advection-driven tendency by surface fluxes. Following a July EDF 2 perturbation, surface fluxes do not balance the initial advective contribution to the same degree, and temperature anomalies in both sectors decay to 50% of their maximum value after a year.

Budget terms for the PmAI index (fig. 3.6) are calculated as the difference between the budget terms for the Pacific basin and those of the Atlantic-Indian basin (left and right columns, respectively, of fig. 3.5). In ECCO, the PmAI time series is primarily a function of positive tendencies due to advection, balanced by negative tendencies due to surface fluxes and, to a lesser extent, diffusion. Time series of budget terms for the PmAI under an EDF 1 perturbation largely resemble those for the Pacific average temperature (fig. 3.5), due to the fact that the temperature tendencies in the Atlantic-Indian are one order magnitude smaller. As is true for Pacific temperature, the PmAI anomaly from the EDF 1 perturbation experiment with respect to ECCO is primarily driven by advection, and decays by 50% in six months following the January 1993 perturbation due to compensatory surface fluxes. Surface fluxes compensate less of the initial perturbation in the July 1992 EDF 1 experiment, resulting in a longer decay time than the January experiment (fig. 3.6e). EDF 2 perturbation experiments result in a slightly smaller impulse response in the PmAI than EDF 1 (fig. 3.6c,e), and decay faster. Like EDF 1, the January perturbation decays faster than the July perturbation due to compensating surface fluxes in the months following the initial perturbation, although the difference in decay following the EDF 2 response between a January and July perturbation is less pronounced than EDF 1.

Having established a seasonality in the ocean's response to the optimal forcing patterns, we investigate the spatial patterns in the temperature response (fig. 3.7a-h). As is evident from the perturbation time series (fig. 3.5), the immediate temperature response to EDF 1 is largely confined to a positive perturbation in the Pacific basin. One year after the forcing perturbation is applied, the temperature response remains confined to the Pacific in regions of large mixed layer depth (fig. 3.7i,j). In the western part of the Pacific sector, wintertime mixed layer depths exceeding 600 meters trap the induced temperature anomalies for longer than a year, especially following a perturbation the previous July. EDF 2 induces positive temperature anomalies in a more confined region of the Pacific, closer to the deep mixed layers shown in fig. 3.7 (i,j), where they largely persist for over a year regardless of the seasonality of the forcing. It appears that the timescale of radiative feedbacks following an EDF 2-like perturbation in the summer is shorter than the timescale of mixed layer deepening, and therefore persistent anomalies in the southwestern Pacific get trapped in the deep mixed layers in the winter following the initial perturbation. While this is also true for EDF 1-like perturbations, the more spatially confined temperature anomalies due to EDF 2 result in less overall decay while the EDF 1-induced anomalies outside of the region of the deepest winter mixed layers decay within a year (fig. 3.7e).

The contribution of wintertime forcing to the PmAI reconstruction (fig. 3.7k) is calculated by setting DPC1 and DPC2 to zero from November through April in all years, and recomputing the convolutions (eq. 3.6); the contribution of summertime forcing is similarly calculated by omitting May through October DPC values. For each DPC, the summertime and wintertime reconstructions sum to the full reconstruction from eq. 3.6. DPC 1 is highly seasonal in its reconstruction: using the wintertime forcing alone recovers 63% of the variance from the full reconstruction, whereas using the summertime forcing only recovers 12%. The covariance between the two seasonal reconstructions accounts for the remaining 25% of variance in the full reconstruction. DPC 2 does not show the same seasonality. The wintertime reconstruction from DPC 2 accounts for 35% of the full variance, while the summertime reconstruction accounts for 24% and the covariance between the two accounts for the remaining 41%.

3.6 Discussion

Local wind stress in the Bellingshausen Sea plays a leading role in driving zonal asymmetries in the upper 700-meter temperature within the Southern Ocean. This is evidenced by compound Dynamics-weighted Principal Component Analysis (DPCA), a novel approach to determining drivers of the ocean by computing optimal forcing patterns in the atmosphere across all variables simultaneously. We have identified two modes that capture 70% of variability across timescales in the zonal temperature asymmetry within the Southern Ocean, as measured by the Pacific minus Atlantic-Indian temperature index (PmAI, *Song et al.* (2024)). The multivariate approach yields modes that are valid across model configurations, resulting in similar variance reduction in an ocean and sea ice model, forced by an atmospheric state, to the linear prediction, despite the adjoint sensitivities themselves having been calculated in the absence of dynamic feedbacks.

The leading forcing mode (EDF 1), with strong wind stress in the Bellingshausen Sea, drives

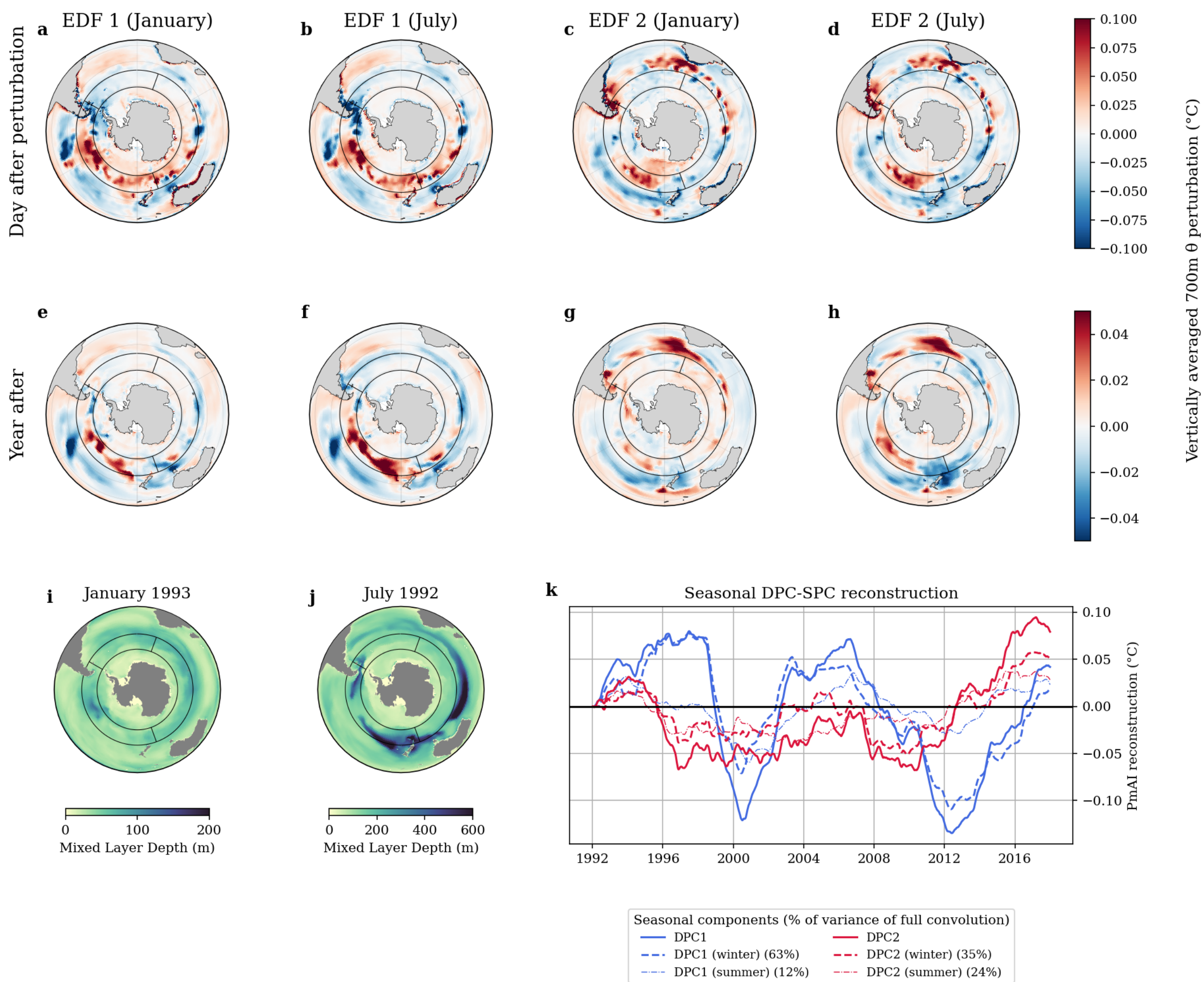

Figure 3.7: (a-h) Maps of upper 700m temperature relative to ECCO for each perturbation experiment, computed the day after the applied perturbation (a-d) and one year after (e-h). (i,j) Mixed layer depths from ECCO output in January 1993 and July 1992, respectively, corresponding to the months in which the forcing perturbations are applied. (k) DPC-SPC reconstructions as in fig. 3.1b, decomposed into seasonal contributions. Percent values indicate variance of each seasonal reconstruction relative to the full DPC-SPC reconstruction. Note that as the seasonal decompositions are not orthogonal in time, their variances do not sum to the full variance.

a strong wintertime response in the Pacific that can account for most of the variability (51%) in the index. EDF 1 has a weaker response in austral summer, which only accounts for 12% of the variance explained by the full mode. We posit that this is due to thermal feedbacks from the relatively shallow summer mixed layer into the atmosphere that outpace the mixed layer deepening in the following winter. EDF 2, with wind stress closer to the western Amundsen Sea southeast of New Zealand and a zonal band of easterly anomalies in the Atlantic-Indian sector, drives an ocean response that is less seasonal and less concentrated in the Pacific. Unlike EDF 1, the response to EDF 2 appears less dependent on mixed-layer seasonality, as the feedbacks following a perturbation are weaker and therefore the mixed layer deepens before the temperature can fully relax. This is likely due to a combination of factors. The induced temperature response in the Pacific is confined to the region of deepest winter mixed layers, where the Pacific-Antarctic ridge also forms a barrier to meridional advection in the northern part of the region (e.g., *Ferster et al.* (2018)). In addition, the zonal band of wind stress in the Atlantic-Indian basin can drive meridional Ekman transport across temperature gradients in all seasons.

The work presented here is consistent with previous findings that changes in local wind stress in the South Pacific over the past several decades have driven asymmetries in upper ocean heating (*Hague et al.* (2024)). While the time series of the PmAI index itself resembles the Interdecadal Pacific Oscillation (IPO) (*Song et al.* (2024)), the adjoint-derived drivers in this study do not show a clear relationship with either the IPO tripolar index or the higher-frequency Niño-3.4 index. The leading EDFs also lack large magnitudes in the tropics (figs. 3.2, 3.3) where these modes primarily manifest. This finding is not necessarily in conflict with previous work, especially given the short (26-year) simulation period that does not resolve many realizations of decadal and longer variability. Rather, it reflects the adjoint sensitivities preferentially weighting local sensitivity in our approach: while the IPO induces large-scale variability in the South Pacific on decadal timescales, the asymmetry in temperature is a function of more regional forcing on all timescales, concentrated near the canonical region of the Amundsen Sea Low.

The concentration of wind stress and sea level pressure near the ASL in the leading EDF patterns (figs. 3.2, 3.3) suggests a strong relationship between the strength and/or position of the ASL and the corresponding temperature asymmetry within the Southern Ocean. The ASL is only weakly correlated with the El Niño-Southern Oscillation (ENSO) in strength and uncorrelated in position (*Turner et al.* (2013)), and is largely driven by planetary waves and storm tracks originating in the midlatitudes (*Raphael et al.* (2016)). The leading DPC modes appear to be stochastic (i.e., lacking spectral peaks), and therefore may be more linked to these stochastic processes driving the ASL than they are to coupled climate modes such as ENSO.

We caveat that the state estimate used in this study spans only 2-3 realizations of decadal variability, with 26 years of simulation, and therefore the exact relationship to known indices cannot be fully discounted. In addition, as the model is not coupled to a dynamical atmospheric model, we cannot investigate the role of perturbations in tropical and subtropical SST in affecting the Southern Ocean through teleconnections, which limits the ability to study the impact of ENSO. Nevertheless, the atmospheric state prescribed in ECCO is derived from reanalysis, and therefore such teleconnections are represented in the base simulation if not in perturbation experiments. Future work using fully coupled models, as well as longer-term state estimates, can further elucidate the role of tropical-extratropical interactions in the local forcing of Southern Ocean temperature asymmetry.

This analysis has corroborated the primacy of forcing in the Pacific sector for driving interannual changes in upper-ocean temperature within the Southern Ocean, and also highlighted that the Atlantic-Indian basin plays an important but second-order role. The exact role of the IPO remains to be investigated within this approach, but it is worth noting that the leading pattern investigated here, which is not highly correlated with the IPO, is sufficient to explain a majority of variance in the zonal asymmetry. Furthermore, the development of compound DPCA and DPC-based linear reconstructions of temperature, which are introduced and validated in this chapter, present a novel method to understand a variety of ocean processes and their external drivers.

Conclusion

The chapters of this dissertation have explored temperature variability in the upper ocean using an array of techniques from numerical modeling, data analysis, and paleoclimate proxies. In Chapter 1, we used a suite of Sea Surface Temperature (SST) proxies in the North Atlantic Ocean and quantified their spectral slope on decadal to centennial timescales in order to better understand how coherent the basin-mean SST reconstruction is. We applied Low-Frequency Component Analysis (LFCA, *Wills et al.* (2018)) to an ensemble of model simulations from the Community Earth System Model (CESM, *Otto-Bliesner et al.* (2016)) and found that leading modes of low-frequency variability can explain some, but not all, of the spatial heterogeneity of spectral slope within the basin; the inherent nonlinearity of the spectral slope also contributes significantly. In Chapter 2, we employed the adjoint to an ocean model, the MITgcm, discovering novel patterns of atmospheric forcing that drive zonal-mean SST variability on interannual timescales within the Southern Ocean. In Chapter 3, we expanded this methodology to explore zonally asymmetric temperature changes of the upper 700 meters of the Southern Ocean, introducing a novel method by which we computed driving atmospheric patterns across all variables, with the finding that wintertime position and strength of the Amundsen Sea Low provides a leading-order control on temperature asymmetry, while summertime westerlies in the Atlantic-Indian basin also contribute a non-negligible component.

The work here has expanded both methodology and physical understanding of the air-sea system, and points to several directions of future work. With the adjoint and compound DPCA methodology developed, we plan to explore sensitivity of SST in the Arctic Ocean to explore optimal sites for inducing sea ice growth as a possible geoengineering strategy. Furthermore, the advent of higher-resolution state estimates allows for a more thorough investigation into the precise atmospheric patterns and air-sea fluxes that drive the ocean, as heat fluxes have been shown to have an important and complex mesoscale structure not resolved in a 1-degree model (e.g., *Gentil et al.* (2026)). Finally, we plan to test the robustness of the forcing patterns found by the DPCA methods in chapters 2 and 3 by applying them to other forced-ocean models.

Bibliography

Adcroft, A., J.-M. Campin, C. Hill, and J. Marshall, Implementation of an Atmosphere–Ocean General Circulation Model on the Expanded Spherical Cube, doi:10.1175/MWR2823.1, 2004.

Allan, E., A. De Vernal, M. F. Knudsen, C. Hillaire-Marcel, M. Moros, S. Ribeiro, M. Ouellet-Bernier, and M. Seidenkrantz, Late Holocene Sea Surface Instabilities in the Disko Bugt Area, West Greenland, in Phase With ^{18} O Oscillations at Camp Century, *Paleoceanography and Paleoclimatology*, *33*(2), 227–243, doi:10.1002/2017PA003289, 2018.

Amrhein, D. E., D. Stephenson, and L. Thompson, A Dynamics-Weighted Principal Components Analysis of Dominant Atmospheric Drivers of Ocean Variability with an Application to the North Atlantic Subpolar Gyre, *Journal of Climate*, *37*(8), doi:10.1175/JCLI-D-23-0197.1, 2024.

Armour, K. C., J. Marshall, J. R. Scott, A. Donohoe, and E. R. Newsom, Southern Ocean warming delayed by circumpolar upwelling and equatorward transport, *Nature Geoscience*, *9*(7), 549–554, doi:10.1038/ngeo2731, 2016.

Berner, K. S., N. Koç, F. Godtliebsen, and D. Divine, Holocene climate variability of the Norwegian Atlantic Current during high and low solar insolation forcing, *Paleoceanography*, *26*(2), 2010PA002,002, doi:10.1029/2010PA002002, 2011.

Cheung, A. H., M. E. Mann, B. A. Steinman, L. M. Frankcombe, M. H. England, and S. K. Miller, Comparison of Low-Frequency Internal Climate Variability in CMIP5 Models and Observations, *JOURNAL OF CLIMATE*, doi:10.1175/JCLI-D-16-0712.1, 2017.

Cunningham, L., et al., NOAA/WDS Paleoclimatology - 1000 Year Composite Sea Surface Temperature Record from the North Atlantic Ocean, doi:10.25921/P44H-7T71.

Deppenmeier, A. L., F. O. Bryan, W. S. Kessler, and L. Thompson, Modulation of cross-isothermal velocities with ENSO in the tropical pacific cold tongue, *Journal of Physical Oceanography*, *51*(5), 1559–1574, doi:10.1175/JPO-D-20-0217.1, 2021.

Deser, C., M. A. Alexander, S.-P. Xie, and A. S. Phillips, Sea Surface Temperature Variability: Patterns and Mechanisms, *Annual Review of Marine Science*, *2*(Volume 2, 2010), 115–143, doi:10.1146/annurev-marine-120408-151453, 2010.

Dong, Y., L. M. Polvani, and D. B. Bonan, Recent Multi-Decadal Southern Ocean Surface Cooling Unlikely Caused by Southern Annular Mode Trends, *Geophysical Research Letters*, *50*(23), e2023GL106,142, doi:10.1029/2023GL106142, _eprint: https://agupubs.onlinelibrary.wiley.com/doi/pdf/10.1029/2023GL106142, 2023.

England, M. H., et al., Recent intensification of wind-driven circulation in the Pacific and the ongoing warming hiatus, *Nature Climate Change*, *4*(3), 222–227, doi:10.1038/nclimate2106, 2014.

Farrell, B. F., and P. J. Ioannou, Generalized Stability Theory. Part I: Autonomous Operators, *Journal of the Atmospheric Sciences*, *53*(14), 2025–2040, doi:10.1175/1520-0469(1996)053<2025:GSTPIA>2.0.CO;2, 1996.

Ferreira, D., J. Marshall, C. M. Bitz, S. Solomon, and A. Plumb, Antarctic Ocean and Sea Ice Response to Ozone Depletion: A Two-Time-Scale Problem, doi:10.1175/JCLI-D-14-00313.1, 2015.

Ferster, B. S., B. Subrahmanyam, I. Fukumori, and E. S. Nyadjro, Variability of Southern Ocean Transports, *Journal of Physical Oceanography*, *48*(11), 2667–2688, doi:10.1175/JPO-D-18-0055.1, 2018.

Fogt, R. L., A. J. Wovrosh, R. A. Langen, and I. Simmonds, The characteristic variability and connection to the underlying synoptic activity of the Amundsen-Bellingshausen Seas Low, *Journal of Geophysical Research: Atmospheres*, *117*(D7), doi:10.1029/2011JD017337, _eprint: https://agupubs.onlinelibrary.wiley.com/doi/pdf/10.1029/2011JD017337, 2012.

Forget, G., D. Ferreira, and X. Liang, On the observability of turbulent transport rates by Argo: supporting evidence from an inversion experiment, *Ocean Science*, *11*(5), 839–853, doi:10.5194/os-11-839-2015, 2015.

Frankignoul, C., and K. Hasselmann, Stochastic climate models, Part II Application to sea-surface temperature anomalies and thermocline variability, *Tellus*, *29*(4), 289–305, doi:10.1111/j.2153-3490.1977.tb00740.x, _eprint: https://onlinelibrary.wiley.com/doi/pdf/10.1111/j.2153-3490.1977.tb00740.x, 1977.

Frölicher, T. L., J. L. Sarmiento, D. J. Paynter, J. P. Dunne, J. P. Krasting, and M. Winton, Dominance of the Southern Ocean in Anthropogenic Carbon and Heat Uptake in CMIP5 Models, *Journal of Climate*, *28*(2), 862–886, doi:10.1175/JCLI-D-14-00117.1, 2015.

Fukumori, I., O. Wang, W. Llovel, I. Fenty, and G. Forget, A near-uniform fluctuation of ocean bottom pressure and sea level across the deep ocean basins of the Arctic Ocean and the Nordic Seas, *Progress in Oceanography*, *134*, 152–172, doi:10.1016/j.pocean.2015.01.013, 2015.

Fukumori, I., O. Wang, and I. Fenty, Causal Mechanisms of Sea Level and Freshwater Content Change in the Beaufort Sea, *Journal of Physical Oceanography*, *51*(10), 3217–3234, doi:10.1175/JPO-D-21-0069.1, 2021.

Gaspar, P., Y. Grégoris, and J.-M. Lefevre, A simple eddy kinetic energy model for simulations of the oceanic vertical mixing: Tests at station Papa and long-term upper ocean study site, *Journal of Geophysical Research: Oceans*, *95*(C9), 16,179–16,193, doi:10.1029/JC095iC09p16179, _eprint: https://agupubs.onlinelibrary.wiley.com/doi/pdf/10.1029/JC095iC09p16179, 1990.

Gebbie, G., Combining Modern and Paleoceanographic Perspectives on Ocean Heat Uptake, *Annual Review of Marine Science*, *13*(1), 255–281, doi:10.1146/annurev-marine-010419-010844, 2021.

Gentil, M., C. de Marez, E. Pallàs-Sanz, A. Bosse, M. Tenreiro, and R. Laxenaire, High-Resolution Observations Unveil (Sub)Mesoscale Heat Fluxes Shaping Upper-Ocean Heat Content, *Geophysical Research Letters*, *53*(8), e2025GL120,922, doi:10.1029/2025GL120922, 2026.

Giering, R., T. Kaminski, and T. Slawig, Generating efficient derivative code with TAF: Adjoint and tangent linear Euler flow around an airfoil, *Future Generation Computer Systems*, *21*(8), 1345–1355, doi:10.1016/j.future.2004.11.003, 2005.

Gong, D., and S. Wang, Definition of Antarctic Oscillation index, *Geophysical Research Letters*, *26*(4), 459–462, doi:10.1029/1999GL900003, _eprint: https://agupubs.onlinelibrary.wiley.com/doi/pdf/10.1029/1999GL900003, 1999.

Hague, M., M. Münnich, and N. Gruber, Zonally Asymmetric Increase in Southern Ocean Heat Content, doi:10.1175/JCLI-D-23-0623.1, 2024.

Hasselmann, K., Stochastic climate models Part I. Theory, *Tellus*, *28*(6), 473–485, doi:10.1111/j.2153-3490.1976.tb00696.x, 1976.

Haumann, F. A., N. Gruber, and M. Münnich, Sea-Ice Induced Southern Ocean Subsurface Warming and Surface Cooling in a Warming Climate, *AGU Advances*, *1*(2), e2019AV000,132, doi:10.1029/2019AV000132, 2020.

Heimbach, P., C. Hill, and R. Giering, An efficient exact adjoint of the parallel MIT General Circulation Model, generated via automatic differentiation, *Future Generation Computer Systems*, *21*(8), 1356–1371, doi:10.1016/j.future.2004.11.010, 2005.

Henley, B. J., J. Gergis, D. J. Karoly, S. Power, J. Kennedy, and C. K. Folland, A Tripole Index for the Interdecadal Pacific Oscillation, *Climate Dynamics*, *45*(11), 3077–3090, doi:10.1007/s00382-015-2525-1, 2015.

Huybers, P., and W. Curry, Links between annual, Milankovitch and continuum temperature variability, *Nature*, *441*(7091), 329–332, doi:10.1038/nature04745, 2006.

Jackson, L. C., A. Biastoch, M. W. Buckley, D. G. Desbruyères, E. Frajka-Williams, B. Moat, and J. Robson, The evolution of the North Atlantic Meridional Overturning Circulation since 1980, *Nature Reviews Earth & Environment*, *3*(4), 241–254, doi:10.1038/s43017-022-00263-2, number: 4, 2022.

Jiang, H., et al., NOAA/WDS Paleoclimatology - Northern North Atlantic Holocene Summer Sea-Surface Temperatures Reconstruction, doi:10.25921/77WA-6N43.

Kamenos, N. A., North Atlantic summers have warmed more than winters since 1353, and the response of marine zooplankton, *Proceedings of the National Academy of Sciences*, *107*(52), 22,442–22,447, doi:10.1073/pnas.1006141107, 2010.

Kang, S. M., Y. Yu, C. Deser, X. Zhang, I.-S. Kang, S.-S. Lee, K. B. Rodgers, and P. Ceppi, Global impacts of recent Southern Ocean cooling, *Proceedings of the National Academy of Sciences*, *120*(30), e2300881,120, doi:10.1073/pnas.2300881120, 2023.

Karoly, D. J., Southern Hemisphere Circulation Features Associated with El Niño-Southern Oscillation Events, *Journal of Climate*, *2*(11), 1239–1252, doi:10.1175/1520-0442(1989)002<1239:SHCFAW>2.0.CO;2, 1989.

Kleeman, R., and A. M. Moore, A Theory for the Limitation of ENSO Predictability Due to Stochastic Atmospheric Transients, *Journal of the Atmospheric Sciences*, *54*(6), 753–767, doi:10.1175/1520-0469(1997)054<0753:ATFTLO>2.0.CO;2, 1997.

Knight, J. R., C. K. Folland, and A. A. Scaife, Climate impacts of the Atlantic Multidecadal Oscillation, *Geophysical Research Letters*, *33*(17), doi:10.1029/2006GL026242, _eprint: https://agupubs.onlinelibrary.wiley.com/doi/pdf/10.1029/2006GL026242, 2006.

Kostov, Y., J. Marshall, U. Hausmann, K. C. Armour, D. Ferreira, and M. M. Holland, Fast and slow responses of Southern Ocean sea surface temperature to SAM in coupled climate models, *Climate Dynamics*, *48*(5), 1595–1609, doi:10.1007/s00382-016-3162-z, 2017.

Kostov, Y., H. L. Johnson, and D. P. Marshall, AMOC sensitivity to surface buoyancy fluxes: the role of air-sea feedback mechanisms, *Climate Dynamics*, *53*(7), 4521–4537, doi:10.1007/s00382-019-04802-4, 2019.

Laepple, T., and P. Huybers, Ocean surface temperature variability: Large model–data differences at decadal and longer periods, *Proceedings of the National Academy of Sciences*, *111*(47), 16,682–16,687, doi:10.1073/pnas.1412077111, 2014.

Laepple, T., et al., Regional but not global temperature variability underestimated by climate models at supradecadal timescales, *Nature Geoscience*, *16*(11), 958–966, doi:10.1038/s41561-023-01299-9, 2023.

Li, Q., and M. H. England, Tropical Indo-Pacific Teleconnections to Southern Ocean Mixed Layer Variability, *Geophysical Research Letters*, *47*(15), e2020GL088,466, doi:10.1029/2020GL088466, _eprint: https://agupubs.onlinelibrary.wiley.com/doi/pdf/10.1029/2020GL088466, 2020.

Lorenz, E., Empirical orthogonal functions and statistical weather prediction, *Statistical Forecasting Project Rep. 1.*, 1956.

Marshall, G. J., Trends in the Southern Annular Mode from Observations and Reanalyses, *Journal of Climate*, *16*(24), 4134–4143, doi:10.1175/1520-0442(2003)016<4134:TITSAM>2.0.CO;2, 2003.

Marshall, J., A. Adcroft, C. Hill, L. Perelman, and C. Heisey, A finite-volume, incompressible Navier Stokes model for studies of the ocean on parallel computers, *Journal of Geophysical Research: Oceans*, *102*(C3), 5753–5766, doi:10.1029/96JC02775, _eprint: https://onlinelibrary.wiley.com/doi/pdf/10.1029/96JC02775, 1997.

Mazloff, M. R., On the Sensitivity of the Drake Passage Transport to Air–Sea Momentum Flux, *Journal of Climate*, *25*(7), 2279–2290, doi:10.1175/JCLI-D-11-00030.1, 2012.

Miettinen, A., D. Divine, N. Koç, F. Godtliebsen, and I. R. Hall, Multicentennial Variability of the Sea Surface Temperature Gradient across the Subpolar North Atlantic over the Last 2.8 kyr*,+, *Journal of Climate*, *25*(12), 4205–4219, doi:10.1175/JCLI-D-11-00581.1, 2012.

Moffa-Sánchez, P., A. Born, I. R. Hall, D. J. R. Thornalley, and S. Barker, Solar forcing of North Atlantic surface temperature and salinity over the past millennium, *Nature Geoscience*, *7*(4), 275–278, doi:10.1038/ngeo2094, 2014.

Moffa-Sánchez, P., et al., Variability in the Northern North Atlantic and Arctic Oceans Across the Last Two Millennia: A Review, *Paleoceanography and Paleoclimatology*, *34*(8), 1399–1436, doi:10.1029/2018PA003508, _eprint: https://onlinelibrary.wiley.com/doi/pdf/10.1029/2018PA003508, 2019.

Moore, G. W. K., J. Halfar, H. Majeed, W. Adey, and A. Kronz, Amplification of the Atlantic Multidecadal Oscillation associated with the onset of the industrial-era warming, *Scientific Reports*, *7*(1), 40,861, doi:10.1038/srep40861, 2017.

Ni, X., L. Du, H. Shi, and Y. Luo, The recent zonal asymmetry of temperature change in the

Antarctic circumpolar current, *Climate Dynamics*, *64*(4), 168, doi:10.1007/s00382-026-08146-8, 2026.

Otto-Bliesner, B. L., E. C. Brady, J. Fasullo, A. Jahn, L. Landrum, S. Stevenson, N. Rosenbloom, A. Mai, and G. Strand, Climate Variability and Change since 850 CE: An Ensemble Approach with the Community Earth System Model, *Bulletin of the American Meteorological Society*, *97*(5), 735–754, doi:10.1175/BAMS-D-14-00233.1, 2016.

Pimm, C., R. G. Williams, D. Jones, and A. J. S. Meijers, Surface Heat Fluxes Drive a Two-Phase Response in Southern Ocean Mode Water Stratification, *Journal of Geophysical Research: Oceans*, *129*(3), e2023JC020,795, doi:10.1029/2023JC020795, _eprint: https://agupubs.onlinelibrary.wiley.com/doi/pdf/10.1029/2023JC020795, 2024.

Prend, C. J., et al., Indo-Pacific Sector Dominates Southern Ocean Carbon Outgassing, *Global Biogeochemical Cycles*, *36*(7), e2021GB007,226, doi:10.1029/2021GB007226, _eprint: https://agupubs.onlinelibrary.wiley.com/doi/pdf/10.1029/2021GB007226, 2022.

Purich, A., G. Boschat, and G. Liguori, Assessing the impact of suppressing Southern Ocean SST variability in a coupled climate model, *Scientific Reports*, *11*(1), 22,069, doi:10.1038/s41598-021-01306-2, 2021.

Raphael, M. N., G. J. Marshall, J. Turner, R. L. Fogt, D. Schneider, D. A. Dixon, J. S. Hosking, J. M. Jones, and W. R. Hobbs, The Amundsen Sea Low: Variability, Change, and Impact on Antarctic Climate, *Bulletin of the American Meteorological Society*, *97*(1), 111–121, doi:10.1175/BAMS-D-14-00018.1, 2016.

Redi, M. H., Oceanic Isopycnal Mixing by Coordinate Rotation, *Journal of Physical Oceanography*, *12*(10), 1154–1158, doi:10.1175/1520-0485(1982)012<1154:OIMBCR>2.0.CO;2, 1982.

Reynolds, D., P. Butler, S. Williams, J. Scourse, C. Richardson, A. Wanamaker, W. Austin, A. Cage, and M. Sayer, A multiproxy reconstruction of Hebridean (NW Scotland) spring sea surface temperatures between AD 1805 and 2010, *Palaeogeography, Palaeoclimatology, Palaeoecology*, *386*, 275–285, doi:10.1016/j.palaeo.2013.05.029, 2013.

Roemmich, D., J. Church, J. Gilson, D. Monselesan, P. Sutton, and S. Wijffels, Unabated planetary warming and its ocean structure since 2006, *Nature Climate Change*, *5*(3), 240–245, doi:10.1038/nclimate2513, 2015.

Russell, J. L., K. W. Dixon, A. Gnanadesikan, R. J. Stouffer, and J. R. Toggweiler, The Southern Hemisphere Westerlies in a Warming World: Propping Open the Door to the Deep Ocean, doi:10.1175/JCLI3984.1, 2006.

Sejrup, H., H. Haflidason, and J. Andrews, A Holocene North Atlantic SST record and regional climate variability, *Quaternary Science Reviews*, *30*(21-22), 3181–3195, doi:10.1016/j.quascirev.2011.07.025, 2011.

Sicre, M., I. R. Hall, J. Mignot, M. Khodri, U. Ezat, M. Truong, J. Eiríksson, and K. Knudsen, Sea surface temperature variability in the subpolar Atlantic over the last two millennia, *Paleoceanography*, *26*(4), 2011PA002,169, doi:10.1029/2011PA002169, 2011.

Sicre, M.-A., et al., Labrador current variability over the last 2000 years, *Earth and Planetary Science Letters*, *400*, 26–32, doi:10.1016/j.epsl.2014.05.016, 2014.

Song, X., Explaining the Zonal Asymmetry in the Air-Sea Net Heat Flux Climatology Over the Antarctic Circumpolar Current, *Journal of Geophysical Research: Oceans*, *125*(6), e2020JC016,215, doi:10.1029/2020JC016215, _eprint: https://onlinelibrary.wiley.com/doi/pdf/10.1029/2020JC016215, 2020.

Song, Y., Y. Li, A. Hu, L. Cheng, G. Forget, X. Chen, J. Duan, and F. Wang, Decadal Thermal

Variability of the Upper Southern Ocean: Zonal Asymmetry, doi:10.1175/JCLI-D-23-0649.1, 2024.

Song, Y., Y. Li, G. Forget, A. Hu, Q. Li, J.-R. Shi, X. Chen, K. Ge, and F. Wang, Inter-basin contrast in the Southern Ocean warming, *Nature Communications*, *16*(1), 9063, doi:10.1038/s41467-025-64112-8, 2025.

Stephenson, D., and F. Sévellec, Dynamical Attribution of North Atlantic Interdecadal Predictability to Oceanic and Atmospheric Turbulence under Diagnosed and Optimal Stochastic Forcing, *Journal of Climate*, *34*(22), 9153–9179, doi:10.1175/JCLI-D-21-0035.1, 2021.

Stephenson, D., D. E. Amrhein, and L. Thompson, Three Atmospheric Patterns Dominate Decadal North Atlantic Overturning Variability, *Geophysical Research Letters*, *51*(18), e2024GL109,193, doi:10.1029/2024GL109193, _eprint: https://onlinelibrary.wiley.com/doi/pdf/10.1029/2024GL109193, 2024.

Talley, L. D., G. L. Pickard, and W. J. Emery (Eds.), *Descriptive physical oceanography: an introduction*, 6th ed ed., Academic Press, Amsterdam ; Boston, oCLC: ocn720651296, 2011.

Thompson, D. W. J., S. Solomon, P. J. Kushner, M. H. England, K. M. Grise, and D. J. Karoly, Signatures of the Antarctic ozone hole in Southern Hemisphere surface climate change, *Nature Geoscience*, *4*(11), 741–749, doi:10.1038/ngeo1296, 2011.

Thomson, D., Spectrum estimation and harmonic analysis, *Proceedings of the IEEE*, *70*(9), 1055–1096, doi:10.1109/PROC.1982.12433, 1982.

Tierney, J. E., and M. P. Tingley, A TEX86 surface sediment database and extended Bayesian calibration, *Scientific Data*, *2*(1), 150,029, doi:10.1038/sdata.2015.29, 2015.

Turner, J., T. Phillips, J. S. Hosking, G. J. Marshall, and A. Orr, The Amundsen Sea low, *International Journal of Climatology*, *33*(7), 1818–1829, doi:10.1002/joc.3558, _eprint: https://rmets.onlinelibrary.wiley.com/doi/pdf/10.1002/joc.3558, 2013.

Wang, L., K. Lyu, W. Zhuang, W. Zhang, S. Makarim, and X.-H. Yan, Recent Shift in the Warming of the Southern Oceans Modulated by Decadal Climate Variability, *Geophysical Research Letters*, *48*(3), e2020GL090,889, doi:10.1029/2020GL090889, _eprint: https://onlinelibrary.wiley.com/doi/pdf/10.1029/2020GL090889, 2021.

Wills, R. C., T. Schneider, J. M. Wallace, D. S. Battisti, and D. L. Hartmann, Disentangling Global Warming, Multidecadal Variability, and El Niño in Pacific Temperatures, *Geophysical Research Letters*, *45*(5), 2487–2496, doi:10.1002/2017GL076327, 2018.

Wills, R. C. J., Y. Dong, C. Proistosecu, K. C. Armour, and D. S. Battisti, Systematic Climate Model Biases in the Large-Scale Patterns of Recent Sea-Surface Temperature and Sea-Level Pressure Change, *Geophysical Research Letters*, *49*(17), doi:10.1029/2022GL100011, 2022.

Yu, L., S. Zhong, C. Sui, and B. Sun, Surface air temperature anomalies over Antarctica and the Southern ocean induced by interactions between the interdecadal Pacific oscillation and Atlantic multidecadal oscillation, *Geoscience Letters*, *11*(1), 39, doi:10.1186/s40562-024-00352-8, 2024.

Zhang, R., R. Sutton, G. Danabasoglu, Y.-O. Kwon, R. Marsh, S. G. Yeager, D. E. Amrhein, and C. M. Little, A Review of the Role of the Atlantic Meridional Overturning Circulation in Atlantic Multidecadal Variability and Associated Climate Impacts, *Reviews of Geophysics*, *57*(2), 316–375, doi:10.1029/2019RG000644, _eprint: https://agupubs.onlinelibrary.wiley.com/doi/pdf/10.1029/2019RG000644, 2019.

Zhong, G., et al., The Southern Ocean carbon sink has been overestimated in the past three decades, *Communications Earth & Environment*, *5*(1), 398, doi:10.1038/s43247-024-01566-6, 2024.

Zhu, F., J. Emile-Geay, N. P. McKay, G. J. Hakim, D. Khider, T. R. Ault, E. J. Steig, S. Dee, and J. W. Kirchner, Climate models can correctly simulate the continuum of global-average temperature variability, *Proceedings of the National Academy of Sciences*, *116*(18), 8728–8733, doi:10.1073/pnas.1809959116, 2019.